Journal of Materials Chemistry C

ROYAL SOCIETY OF CHEMISTRY

PAPER

View Article Online
View Journal | View Issue

Cite this: J. Mater. Chem. C, 2024, 12, 9716

Synergy between structural rigidity and cluster defects in a bright near-infrared Cr^{3+}-based phosphor for excellent thermal stability and long afterglow†

Annu Balhara,[ab] Santosh K. Gupta,*[ab] Brindaban Modak,[be] Malini Abraham,[cd] Ashok Kumar Yadav,[f] Harshini V. Annadata,[f] Subrata Das,[cd] Narender Singh Rawat[bg] and Kathi Sudarshan[ab]

Received 15th April 2024,
Accepted 29th May 2024

DOI: 10.1039/d4tc01530d

rsc.li/materials-c

Near-infrared (NIR) phosphor-converted light-emitting diodes (pc-LEDs) driven by blue LEDs have emerged as promising future NIR light sources with high energy efficiency and compact structure for applications in medical diagnosis, night vision, and agriculture. However, development of thermally robust NIR light sources presents a great challenge. Herein, we report a blue light-pumped $Y_3Al_2Ga_3O_{12}:Cr^{3+}$ phosphor with thermally stable broadband NIR emission (105% at 423 K) and a high quantum efficiency of 76%, covering the range from 630 to 950 nm. Moreover, the $Y_3Al_2Ga_3O_{12}:Cr^{3+}$ phosphor displayed long persistent luminescence (PersL) under UV charging. Synchrotron based extended X-ray absorption fine structure (EXAFS) indicated the octahedral Cr^{3+} lattice sites and local structure. Low temperature-dependent EXAFS studies revealed rigid octahedral coordination of Cr^{3+} ions at Al/GaO_6 sites with minimal thermally activated distortion even in the second/third coordination shell. The lattice stiffness resulted in superior temperature-dependent NIR photoluminescence properties (80 to 433 K) with abnormal anti-thermal quenching desirable for pc-LEDs at 150 °C. Furthermore, the intrinsic defects were probed using positron annihilation lifetime spectroscopy and density functional theory, which suggested feasible formation of oxygen vacancies (V_O) and cluster defects ($V_{Al/Ga}$–V_O). Introduction of abundant traps with wide-ranging trap depths (~0.7 to 1 eV) facilitated the long PersL with UV charging and defect activated thermal stability. Finally, the fabricated NIR pc-LED device exhibits efficient electroluminescence and its potential applications in imaging and night vision were demonstrated. Then, promising long PersL of the fabricated thin film under X-ray charging is presented. This work investigates the application prospects and highlights the important structural and defect related dynamics of this promising phosphor for NIR pc-LED devices.

1. Introduction

In recent years, near-infrared (NIR) light emitting phosphors have attracted widespread research attention due to their applications in security, night vision, surveillance technology, biomedicine, environmental monitoring, optical communication, food analysis, agriculture, *etc.*[1–3] The current research focus is on designing efficient broadband NIR phosphor-

[a] Radiochemistry Division, Bhabha Atomic Research Centre, Trombay, Mumbai 400085, India. E-mail: santoshg@barc.gov.in, santufrnd@gmail.com
[b] Homi Bhabha National Institute, Anushaktinagar, Mumbai 400094, India
[c] Materials Science and Technology Division, CSIR-National Institute for Interdisciplinary Science and Technology, Thiruvananthapuram, Kerala 695019, India
[d] Academy of Scientific and Innovative Research (AcSIR), Ghaziabad 201002, India
[e] Chemistry Division, Bhabha Atomic Research Centre, Trombay, Mumbai 400085, India
[f] Beamline Development & Application Section, Bhabha Atomic Research Centre, Mumbai 400085, India
[g] Radiological Physics and Advisory Division, Bhabha Atomic Research Centre, Trombay, Mumbai 400085, India

† Electronic supplementary information (ESI) available: Characterization techniques, EXAFS experimental details, computational details, EDS spectra, XANES and Fourier transform EXAFS spectra at Y and Ga K-edges, tables showing EXAFS results with bond lengths, coordination number and disorder parameter values at Y and Ga K-edges, PL emission spectra at 80 K, quantum yield spectra, EPR spectra at 100 K, emission decay curves and lifetime values, PALS lifetime plots, table showing defect formation energies, density of states plots, defect level diagram, phonon dispersion plot, XPS spectrum, and elemental mapping and PL of thin film. See DOI: https://doi.org/10.1039/d4tc01530d

converted light emitting diodes (pc-LEDs) as ideal alternatives for halogen lamps, laser diodes, incandescent bulbs, and IR LEDs. These conventional sources have irreparable shortcomings such as large size, high energy consumption, shorter lifetimes, low efficiency, and high cost.[1,2] The quest for developing NIR pc-LEDs is inspired by their incomparable superiority over traditional NIR light sources through a combination of compact size, longer life, lower energy consumption and broad emission.[2–5] Therefore, development of broadband NIR light emitting phosphors with broadband emission and high thermal stability, output power, efficient photoluminescence quantum yield (PLQY), and high photoelectric conversion is preferable for NIR pc-LED applications. Adding to this, long NIR persistent luminescence (PersL) enlarges the sphere of applications including safe *in vivo* bioimaging, anticounterfeiting, safety signals and emergency lighting, luminous paint, night-vision surveillance, *etc.*[6]

Currently, the Cr^{3+} ion is the preferred choice for an ideal NIR activator among other transition metals owing to its broadband NIR emission originating from 3d–3d electronic transitions and efficient absorption in the blue region.[7] The emission of Cr^{3+} ions is decided by crystal field strength as d orbitals are sensitive to the local structure.[8] Hence, host selection is the critical step for incorporating Cr^{3+} as an emission center to develop broadband NIR pc-LEDs. Cr^{3+} in octahedral sites is well known to be a far red/NIR emitting center.[9] Cr^{3+} exhibits sharp emission (~700 nm) due to spin-forbidden $^2E \rightarrow {}^4A_{2g}$ transition, and the broad emission is attributed to spin-allowed $^4T_{2g} \rightarrow {}^4A_{2g}$ transitions with the tunable emission range of 650–1600 nm.[10,11] Importantly, the absorption band due to $^4A_{2g} \rightarrow {}^4T_{1g}$ transition matches aptly with blue LED chips. Therefore, the host materials offering octahedral coordination for Cr^{3+} and weak crystal field have gained significant attention in recent years. Representative phosphors with shorter and longer emission wavelengths include $YGa_3(BO_3)_4:Cr^{3+}$,[12] $BaAl_4Sb_2O_{12}:Cr^{3+}$,[13] $Ga_2O_3:Cr^{3+}$,[14] $Na_2CaGe_6O_{14}:Cr^{3+}$,[15] $Ga_4GeO_8:Cr^{3+}$,[16] $CaLu_2Al_4SiO_{12}$,[17] $Li_3Mg_2NbO_6:Cr^{3+}$,[18] $SrGa_2O_4:Cr^{3+}$,[19] *etc.* Over recent years, substantial progress has been made in developing Cr^{3+}-based long PersL phosphors and investigating the mechanism of afterglow.[1,2,15,20] Huang and co-workers[21] designed a Cr^{3+}-doped $Na_{0.5}Gd_{0.5}TiO_3$ NIR-PersL phosphor and investigated charging mechanisms using theoretical calculations. Taktak *et al.*[22] reported $Zn_2SnO_4:Cr^{3+}$ spinel phosphors showing long NIR PersL. Ding's group[15] developed $Na_2CaGe_6O_{14}:Cr^{3+}$ phosphors, which displayed broadband NIR PersL for ~10 h.

Garnet phosphors ($A_3B_2C_3O_{12}$) are the hotspot matrices for Cr^{3+} doping due to the presence of multiple cation sites ([A], [B], and [C] cations in dodecahedral, octahedral, and tetrahedral coordination sites) with tunable crystal field and rigid structure.[1,23–27] A large number of reports published so far on Cr^{3+}-based garnet phosphors demonstrated NIR broadband emission with high efficiency and thermal stability, which are the basic prerequisites for designing advanced NIR light sources. For example, Wang *et al.*[28] reported Cr^{3+} doped $Ca_3Sc_2Ge_3O_{12}$ broadband NIR phosphors with high thermal stability (~97% at 100 °C) and an internal quantum efficiency (IQE) of 61%. Jiang *et al.*[23] synthesized $Gd_3ScMgGa_2SiO_{12}:Cr^{3+}$ phosphors with a full width at half maximum (FWHM) of 150 nm, an IQE of 90% and good thermal stability (~85.3 at 150 °C). Li *et al.*[29] reported high IQE (74%) and near-zero thermal quenching (~97% at 423 K) for a $Y_3Sc_2Al_3O_{12}$ garnet phosphor. Recently, Li *et al.*[30] reported a $Y_3In_2Ga_3O_{12}:Cr^{3+}$ phosphor with an IQE of 91.6%, a FWHM of 125 nm and zero thermal quenching (100% at 150 °C). However, the robust NIR emission was proposed due to traps but no solid proof was provided to explain the defect induced thermal stability. Other previously reported Cr^{3+} phosphors for pc-LEDs include $Ca_3Sc_2Ge_3O_{12}:Cr^{3+},Ce^{3+}$ with good thermal stability (IQE = 22%),[28] $Gd_{2.4}Lu_{0.6}Ga_4AlO_{12}:Cr^{3+}$ with a high IQE of ~90% and low thermal stability (75% at 423 K),[5] $Ca_2YHf_2Al_3O_{12}:Cr^{3+}$ (90% at 423 K and IQE ~ 75%),[27] *etc.* Similarly, $Y_3Al_2Ga_3O_{12}$ (YAGG) is a well-known host matrix demonstrating good PLQY, thermal stability, rigid structure and accommodation of transition metals at multiple sites.[6,31–34] Based on earlier reports, $Y_3Al_2Ga_3O_{12}$ is the optimal composition among the solid-solutions of the $Y_3Al_{5-x}Ga_xO_{12}:Cr^{3+}$ (x = 0 to 5) garnet, which displayed ideal luminescence properties with intermediate crystal field strength.[2,35]

Although Cr^{3+}-activated garnet phosphors have been widely explored for NIR pc-LEDs, the luminescence mechanism, thermal stability, origin of defects, site-occupation and structure–property relationship of garnets lack a clear understanding. In addition, thorough investigation of structural rigidity and defects resulting in thermal stability, long afterglow, and thermally induced Cr^{3+} local structural changes in the garnet matrix is lacking. Most of these reports investigated the thermal stability in the optimum pc-LED range, PLQY, crystal field variation and thermoluminescence properties in detail. Importantly, the thermal stability is often attributed to intrinsic defects and rigidity of the host matrix without much attention to their origin. Consequently, achieving good thermal stability with desired PLQY remains a problem for fast advancement of high-power NIR pc-LEDs. Additionally, the changes in the emission peak profile at elevated temperatures pose a strong hindrance. Generally, the mechanism of long PersL is explained on the basis of trap information derived from thermoluminescence studies. Despite a handful of reports, the understanding of trap types, feasibility of formation of traps and their position in between the bandgap is unclear in the majority of reported long PersL phosphors. Understanding the thermally induced structural distortions and distribution of Cr^{3+} ions and defects in garnet materials will be crucial for development of next generation NIR phosphors for lighting and bio-medical applications. Hence, in this work, we carried out an in-depth experimental and theoretical investigation of changes in the local structure, types of traps, defect formation energies, and temperature-dependent structural distortions, which will help to unfold the mechanism of thermal quenching.

In this study, we synthesized a series of $Y_3Al_2Ga_3O_{12}:xCr^{3+}$ (x = 0.02, 0.04, 0.06, 0.10 and 0.30 mol) NIR garnet phosphors using a solid state route. The Cr^{3+} doped $Y_3Al_2Ga_3O_{12}$ phosphor demonstrated high thermal stability (~105% at 423 K) and an IQE of ~76%, which are important parameters for NIR pc-LEDs. Furthermore, low temperature dependent synchrotron-

based extended X-ray absorption fine structure (EXAFS) investigation provided useful insights into rigid coordination of Cr^{3+} ions in the YAGG matrix, which is desirable for thermally robust luminescence. The temperature-dependent structural distortions were evaluated using temperature-dependent EXAFS studies. The low and high temperature-dependent photoluminescence (PL) studies showed increase in FWHM and overall integrated intensity without much change in peak positions, which revealed thermal population of $^4T_2$ states. Moreover, the explanation of thermal stability is discussed based on thermoluminescence (TL), density functional theory (DFT) calculations, and positron annihilation lifetime spectroscopy (PALS) studies. The association between Cr^{3+} local structure, crystal field, NIR PL properties, and mechanism of thermal stability and PersL is well established benefiting from advanced EXAFS, PALS, and DFT calculations. Furthermore, we fabricated a YAGG:Cr^{3+} phosphor based NIR LED device with efficient broadband electroluminescence (EL) in the range of 630–950 nm and investigated power-dependent EL spectra of pc-LEDs. Additionally, $Y_3Al_2Ga_3O_{12}$:Cr^{3+} phosphors/PMMA thin films were fabricated to demonstrate the moisture-stable PL and persistent luminescence. The results obtained in this study highlight key structural and luminescence properties, which will accelerate the current development pace of NIR pc-LEDs.

2. Results and discussion

2.1 Crystal structure, morphology and oxidation state

Fig. 1(a) shows the X-ray diffraction (XRD) patterns of YAGG:$x$$Cr^{3+}$ (x = 0.02, 0.04, 0.06, 0.10 and 0.30 mol) samples. The diffraction peaks observed in the XRD patterns of pure YAGG and Cr^{3+}-doped YAGG samples match well with the standard data (ICSD code: 280107). This suggested the formation of pure phase upon doping Cr^{3+} ions into the YAGG crystal lattice without the formation of any impurity phase. The crystal structure of $Y_3Al_2Ga_3O_{12}$ and coordination of each cation site are presented in Fig. 1(b), where the Y^{3+} ions occupy dodecahedral sites and Al^{3+} and Ga^{3+} occupy the octahedral and tetrahedral sites, with a higher feasibility of Ga^{3+} ions occupying the tetrahedral sites. Laguta *et al.*[36] experimentally determined the distribution of Al^{3+} and Ga^{3+} ions in $Y_3Al_2Ga_3O_{12}$ and reported that 72% of the Ga^{3+} ions has tetrahedral coordination and 28% occupy octahedral sites. The Cr^{3+} ion can occupy the Al^{3+}/Ga^{3+} octahedral sites as the ionic radii of Cr^{3+} ions (0.615 Å) are comparable with ionic radii of Al^{3+} (0.535 Å) and Ga^{3+} (0.62 Å) ions.[37]

Fig. 1(c) shows the FTIR spectra of Cr^{3+} doped YAGG samples and no significant changes in the vibrational frequencies were observed upon incorporation of Cr^{3+} ions. The vibrational bands observed between 570 and 830 cm^{-1} can be assigned to Ga–O and Al–O stretching frequencies in the YAGG

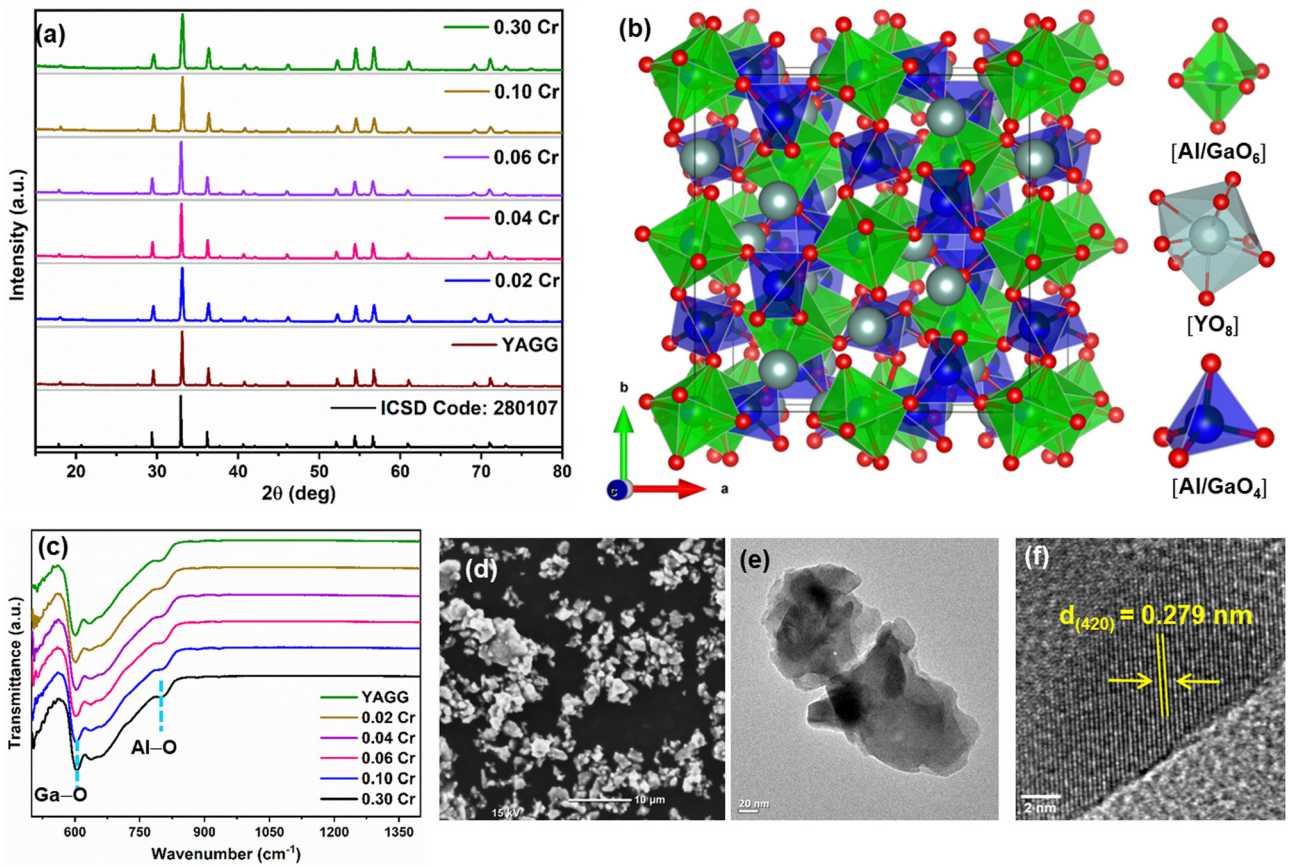

Fig. 1 (a) XRD patterns of YAGG:$x$$Cr^{3+}$ (x = 0.02, 0.04, 0.06, 0.10 and 0.30 mol) samples. (b) Crystal structure of $Y_3Al_2Ga_3O_{12}$, (c) FTIR spectra. (d)–(f) SEM, TEM, and HRTEM images of the YAGG:0.04Cr^{3+} phosphor, respectively.

lattice.[38,39] The scanning electron microscopy (SEM) image of YAGG:0.04Cr^{3+} confirmed the formation of micron size YAGG particles with irregular morphology (Fig. 1(d)). The EDS spectra reveal the presence of Y, Al, Ga, Cr, and O elements and successful incorporation of Cr^{3+} ions (Fig. S1 in ESI†). Fig. 1(e) and (f) show the TEM and HRTEM images of the YAGG:0.04Cr^{3+} sample. The *d*-spacing of ~ 0.279 nm observed in the HRTEM image is due to the (420) crystallographic plane of YAGG.

2.2 Oxidation state of Cr and local structure

X-ray absorption near edge structure (XANES) measurements have been carried out at three absorption sites namely Y, Ga and Cr K-edges. The normalised XANES spectra of Cr, Y, and Ga along with their respective standards are shown in Fig. 2(a) and Fig. S2a, b (ESI†). It is evident that both probe elements (Ga and Y) exhibit trivalent states in all the samples, as confirmed by the alignment of their absorption edge positions with the respective trivalent standards. The absorption edge position (at the half absorption jump) of Cr doped YAGG samples appears at a relatively higher energy side; however, their white line peak positions around 6011 eV coincide. Farges *et al.*[40] concluded that determining the chromium valence based on the position of the edge jump region was not straightforward, as the main jump energy could vary by up to 2.6 eV in five model compounds with trivalent chromium octahedrally coordinated to oxygen ligands.[40] Consequently, an alternative approach has been suggested, which involves analysing the pre-edge region, specifically around 5994 eV. The position and intensity of localized transitions observed at the K pre-edge are recognized indicators of the chromium oxidation

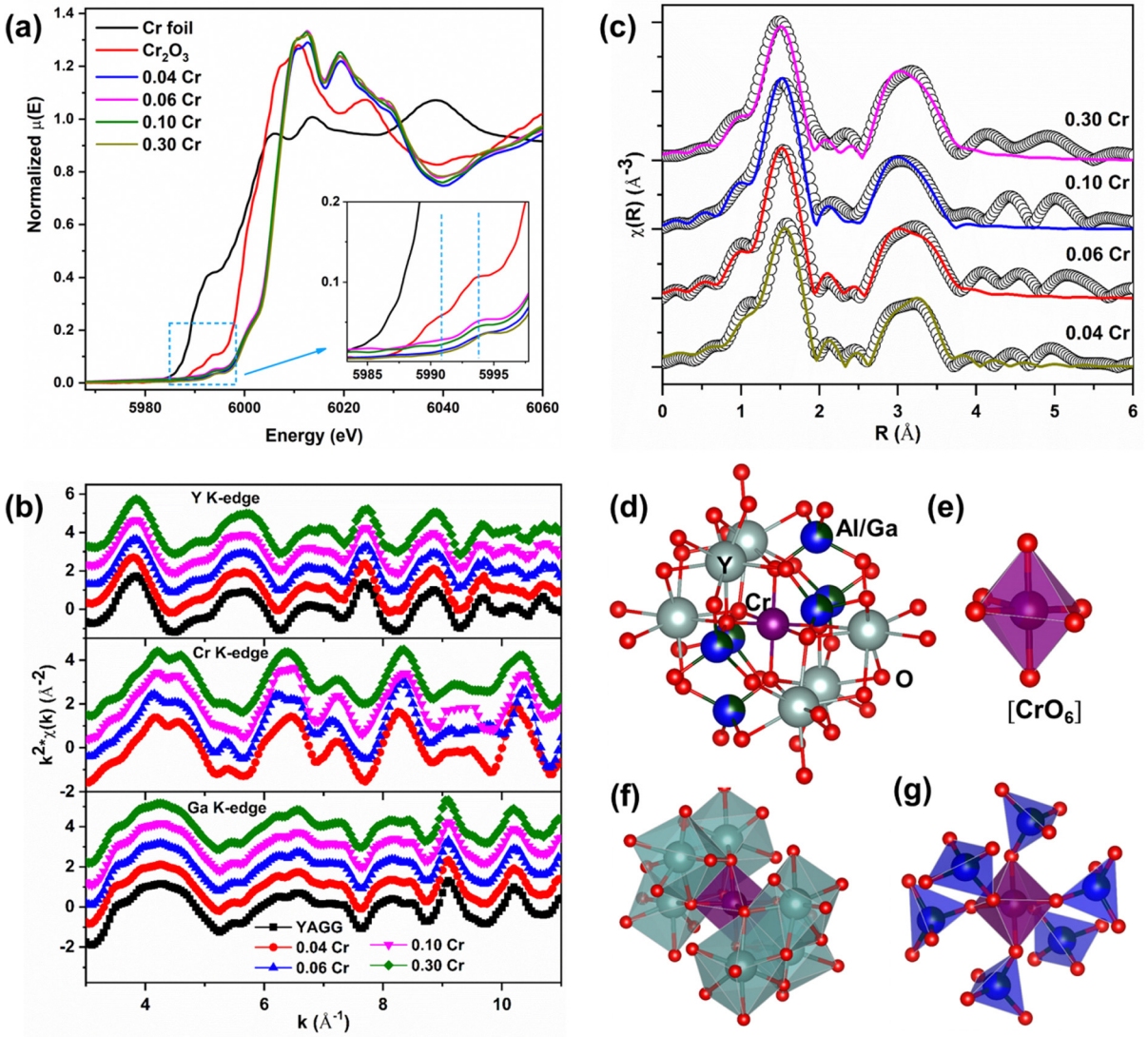

Fig. 2 (a) Normalised XANES spectra at the Cr K-edge along with that of Cr foil and Cr_2O_3 standards. (b) EXAFS oscillations in wave vector space at the Y K-edge, Cr K-edge and Ga K-edge, respectively. (c) Fourier transform EXAFS spectrum (scatter points) and the respective fittings (solid line) of Cr doped YAGG at the Cr K-edge. The spectra are vertically shifted for better visualisation. (d) Local structure of Cr^{3+} ions. (e) Octahedral coordination of Cr^{3+} ions. (f) The second coordination environment of Cr^{3+} ions surrounded by YO_8 units. (g) The third coordination environment of Cr^{3+} ions surrounded by Al/GaO_4 units.

state and the geometry of its surrounding environment.[40] In the case of trivalent Cr_2O_3 doublet pre-peaks are observed, particularly well-resolved when chromium is in a trivalent state. The inset of Fig. 2(a) shows that the position of the pre-edge in Cr doped YAGG samples coincides with the pre-edge peaks of Cr_2O_3, confirming the trivalent state in the samples. This doublet typically arises from quadrupolar 1s to 3d transitions resulting from the hybridization of Cr 3d levels in the presence of neighbouring oxygen ligands.[41–43]

The low pre-edge peak intensity of Cr doped YAGG samples reveals octahedral coordination, indicating that the Cr sites have centrosymmetry and prohibit the hybridization. Local structural information has been extracted by analysing the EXAFS region of the absorption spectra. The EXAFS oscillations, depicted in Fig. 2(b) at the Y, Ga, and Cr K-edges after removing the bare atom background, are presented for examination. These oscillations can serve as valuable tools for the quantitative analysis of the spectra. The EXAFS oscillations at the Cr K-edge (Fig. 2(b)) exhibit a notable similarity to the Ga K-edge oscillations when compared to the Y K-edge EXAFS oscillations. As we discussed above, Ga can exist in both tetrahedral and octahedral coordination sites. The EXAFS oscillations depicted in Fig. 2(b) suggested a combination of both. Based on the obtained coordination (close to 4 instead of 6), we concluded that Ga is likely to prefer tetrahedral sites. Based on the obtained Cr–O coordination number (close to 6), we predicted them to be present at octahedral sites. We would also like to clarify that while the EXAFS oscillations of Cr are not identical to those of Ga, they are similar. The coordination number primarily affects the amplitude of the oscillations when bond lengths are quite similar. The resemblance in EXAFS oscillations between Cr and Ga can be attributed to their comparable bond lengths (1.98 Å for Cr and 1.85 Å for Ga, instead of the larger 2.32 Å). It is reasonable to expect the oscillations to be similar to Ga. Additionally, the contributions of other coordination shells to the oscillations should be similar to Ga rather than Y. This observation suggests the substitution of Cr ions at octahedral Ga/Al crystallographic sites.

The $\chi(R)$ *versus* R plots, derived from the Fourier transform of $\chi(k)$ spectra, are illustrated in Fig. S3 (ESI†) at the Y, Ga, and Cr K-edges. The displayed Fourier transform spectra are not phase-corrected, leading to the coordination peak in these spectra appearing at slightly lower inter-atomic distances (R) in comparison to the actual bond length. Upon visual inspection of the Fourier transform spectra at the Ga, Y, and Cr K-edges, it is apparent that the Cr spectra exhibit a notable similarity to the Ga K-edge spectra. The outcomes of the fitting process are presented in Table 1 and Tables S1, S2 (ESI†), and the optimal fitting spectra are illustrated in Fig. S4 and S5 (ESI†). Although Y^{3+} ions typically occupy dodecahedral sites with eight-coordinate geometry, this coordination is spread across two adjacent coordination shells. The Y–O coordination is represented by two nearby distances of 2.32 Å and 2.45 Å, as shown in Table S1 (ESI†). The noteworthy findings are evident in the Cr K-edge results, as displayed in Fig. 2(c).

The Cr ions situated at substitutional sites exhibit octahedral coordination, a conclusion substantiated by the discernible

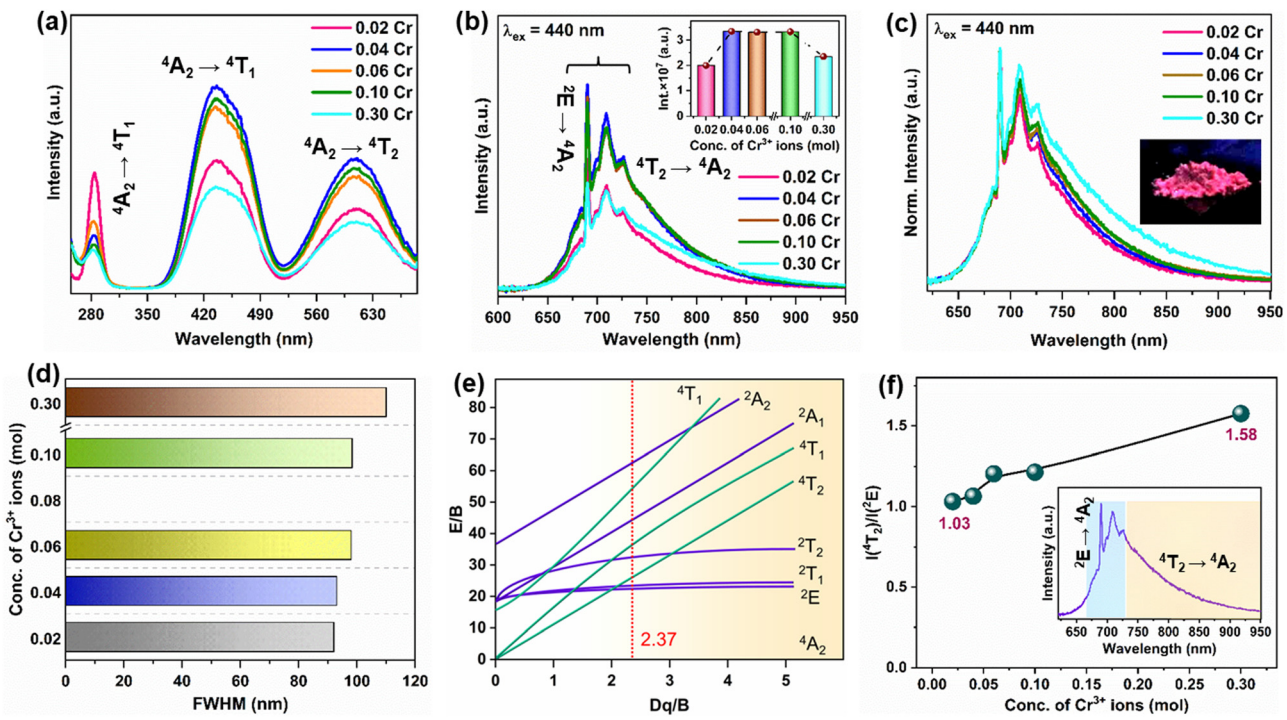

Fig. 3 (a) PLE spectra of YAGG:xCr^{3+} (x = 0.02–0.30 mol) phosphors at room temperature. (b) PL emission spectra and the integral intensities as a function of Cr^{3+} concentrations (inset). (c) Normalized PL emission spectra and emission photograph of the YAGG:0.04Cr phosphor under UV light (inset). (d) FWHM as a function of Cr^{3+} concentrations. (e) Schematic of the Tanabe–Sugano (T–S) energy level diagram for octahedrally coordinated Cr^{3+} ions. (f) Variation of $I(^4T_2)/I(^2E)$ with Cr^{3+} doping content and emission bands for ^2E and $^4T_2$ levels (inset).

Table 1 Bond length, coordination number and disorder factor obtained by EXAFS fitting at the Cr K-edge

Path	Parameters	YAGG:2% Cr	YAGG:3% Cr	YAGG:5% Cr	YAGG:15% Cr
Cr–O	R (Å)	1.98 ± 0.01	1.99 ± 0.02	1.98 ± 0.02	2.00 ± 0.01
	N	5.77 ± 0.32	6.02 ± 0.52	5.77 ± 0.25	5.53 ± 0.21
	σ^2 (Å^2)	0.0022 ± 0.0009	0.0020 ± 0.0012	0.0021 ± 0.0013	0.0020 ± 0.0015
Cr–Y	R (Å)	3.49 ± 0.01	3.47 ± 0.02	3.47 ± 0.02	3.49 ± 0.02
	N	5.76 ± 0.25	6.02 ± 0.35	5.79 ± 0.39	5.53 ± 0.35
	σ^2 (Å^2)	0.0187 ± 0017	0.0110 ± 0014	0.0172 ± 0011	0.0159 ± 0017
Cr–Al/Ga	R (Å)	3.49 ± 0.02	3.47 ± 0.02	3.47 ± 0.02	3.49 ± 0.02
	N	5.76 ± 0.25	6.02 ± 0.35	5.79 ± 0.39	5.53 ± 0.35
	σ^2 (Å^2)	0.0015 ± 0.0016	0.0018 ± 0.0016	0.0021 ± 0.0016	0.0037 ± 0.0011

features observed in XANES measurements. The EXAFS oscillations in K-space discussed earlier signify the presence of Cr at Al/Ga sites, with the subsequent EXAFS results identifying an octahedral site preferred by Cr ions. The local structure of Cr^{3+} ions with the second and third coordination shells is presented in Fig. 2(d)–(g). The determined coordination number decisively precludes the possibility of Cr occupying tetrahedral sites, yielding a compelling result. This observation is particularly intriguing. The preference for the octahedral site can be rationalized by considering the analogous ionic radii of trivalent Cr in octahedral coordination (0.615 Å) with trivalent Ga ions in octahedral coordination (0.62 Å), in contrast to tetrahedral coordination (0.47 Å).[44]

2.3 Photoluminescence studies

The PLE spectra of Cr^{3+} doped YAGG phosphors monitored at 690 nm emission are shown in Fig. 3(a), in which three excitation bands were observed at 280 nm, 440 nm, and 610 nm, which can be ascribed to the spin-allowed $^4A_2 \rightarrow {}^4T_1$ (^4P), $^4A_2 \rightarrow {}^4T_1$ (^4F) and $^4A_2 \rightarrow {}^4T_2$ (^4F) transitions of Cr^{3+} ions, respectively.[45,46] Fig. 3(b) displays the concentration-dependent PL emission spectra of Cr^{3+} doped YAGG phosphors upon blue light excitation at 440 nm. The $^2E \rightarrow {}^4A_2$ transition results in a sharp-line emission peak at 690 nm (R-line), and the intense broadband NIR emission in the range of 630–950 nm can be attributed to $^4T_2 \rightarrow {}^4A_2$ transition.[45,46] The comparison of PL emission spectra of the YAGG:0.04Cr phosphor recorded at 80 K and room temperature is shown in Fig. S6 (ESI†). At low-temperature, the sharp-line emission from ^2E states is dominant. The Stokes and anti-Stokes phonon sidebands of the R-line can be seen in the PL emission spectrum over a broad emission band at 710 and 725 nm at 80 and 300 K.[13] At room temperature, the overlap of the broadband $^4T_2$ emission band and phonon sidebands at 710 nm and 725 nm is observed with increment in $^4T_2$ emission while the sharp ^2E emission decreased sharply.

The maximum integrated emission intensity was observed at x = 0.04 (inset of Fig. 3(b)), and further increment in Cr^{3+} doping content ($x \geq 0.06$) led to decreased PL intensity due to concentration quenching. The IQE of YAGG:0.04Cr^{3+} is 76% (Fig. S7, ESI†), which confirmed high luminous efficiency of Cr^{3+}-doped YAGG phosphors. The emission photograph of the YAGG:0.04Cr phosphor under UV light is provided in the inset of Fig. 3(c). It is well reported that the luminescence of Cr^{3+} is significantly influenced by the crystal field.[47] The presence of emission bands due to both $^2E/{}^4T_2 \rightarrow {}^4A_2$ transitions revealed the incorporation of Cr^{3+} ions in octahedral sites with intermediate crystal field strength. We evaluated the crystal field strength (Dq) and Racah parameter (B) of the Cr^{3+} sites in the YAGG:0.04Cr^{3+} sample by using the following equations:[48]

$$Dq/B = 15(x - 8)/x^2 - 10x \quad (1)$$

$$Dq = E(^4A_2 - {}^4T_1)/10 \quad (2)$$

$$x = E(^4A_2 \rightarrow {}^4T_1) - E(^4A_2 \rightarrow {}^4T_2)/Dq \quad (3)$$

where the x value was calculated by using the average peak energies of the $^4A_2 \rightarrow {}^4T_1/{}^4T_2$ transitions of Cr^{3+} ions.[14] Fig. 3(e) displays the Tanabe–Sugano (T–S) diagram with located crystal field strength and energy level positions of Cr^{3+} ions in octahedral coordinated Al/GaO_6 sites in the YAGG matrix. Accordingly, the Dq/B, Dq, and B values were determined as 2.37, 1523.9 cm^{-1}, and 642 cm^{-1}, respectively. Based on the T–S diagram, the $^4T_2$ energy level is slightly higher in energy than ^2E due to which the dominant sharp-line emission along with broad NIR emission is observed for all Cr^{3+}-doped YAGG phosphors. Two regions were selected to evaluate the integrated intensity of $^4T_2$ and ^2E emission bands[17] (see the inset of Fig. 3(f)). An increasing trend was observed for the $I(^4T_2)/I(^2E)$ values calculated as a function of Cr^{3+} doping content in Fig. 3(f).

No changes were noticed in the peak positions of excitation and emission bands in concentration-dependent PLE and PL emission spectra of Cr^{3+} doped YAGG phosphors. This revealed that increasing content of Cr^{3+} has a negligible effect on the crystal field of Cr^{3+} ions. This was supported by intact Cr–O bonds of Cr^{3+} ions in Al/GaO_6 octahedral sites, as no significant changes were observed in bond lengths and disorder values (σ^2) in the EXAFS analysis (Table 1). The normalized PL emission as a function of Cr^{3+} doping concentration is shown in Fig. 3(c). It is noteworthy that the PL emission became broader (Fig. 3(c)) and the FWHM of emission band increased from 44 to 72 nm (see Fig. 3(d)) with increase in doping concentration of Cr^{3+} ions (x = 0.02 to 0.30 mol). Here, the increased FWHM cannot be explained by changes in the crystal field generally accounted in the previous reports.[1] This may be attributed to the increasing electron–phonon coupling (EPC) effect in the YAGG lattice.[49] EPR is a hypersensitive technique used to gain useful information about the local structure of Cr^{3+} ions. The EPR spectra of all the Cr^{3+} doped YAGG samples were recorded at 100 K to gain insights into the local structure of Cr^{3+} ions in the YAGG lattice

(see Fig. S8, ESI†). Two EPR signals were observed at $g \sim 3.75$ and $g \sim 1.98$, which can be attributed to isolated Cr^{3+} ions in octahedral coordination and Cr^{3+}–Cr^{3+} pairs, respectively, based on the available literature.[30,49] The formation of Cr^{3+}–Cr^{3+} ion pairs is more feasible at higher Cr^{3+} doping content, and therefore, these pairs contribute significantly to the increased tail-like emission at higher wavelengths (>800 nm).[17] The probable electron migration from ^2E to $^4T_2$ energy levels between neighbouring Cr^{3+} ions is expected to increase with increment in Cr^{3+} concentration, which results in thermal population of the $^4T_2$ energy state.

Room temperature luminescence decay profiles were recorded for Cr^{3+}-doped YAGG phosphors under 440 nm excitation, monitoring emissions at 690, 710, and 750 nm (Fig. 4(a) and (b) and Fig. S9, ESI†). The average lifetimes (τ_{avg}) were calculated by fitting the excited state decay curves with a bi-exponential decay function:

$$I(t) = I_0 + A_1 e^{-t/\tau_1} + A_2 e^{-t/\tau_2} \quad (4)$$

where I_0 and $I(t)$ represent the emission intensities at zero offset and at 't' time, respectively, τ_1 and τ_2 are the two lifetime components, and A_1 and A_2 are constants. The lifetime values for different emission peak positions of Cr^{3+}-doped YAGG phosphors are summarized in Table S3 (ESI†). The average lifetimes of the 690 nm emission peak decreased significantly from 477.6 to 263.5 μs upon increasing the Cr^{3+} doping concentrations (x = 0.02 to 0.30) (Fig. 4(a)). Similarly, the lifetime values of 750 nm peaks decreased from 445.4 to 257.8 μs (Fig. 4(b)). This decreasing lifetime trend indicated a higher probability of non-radiative relaxation processes at higher Cr^{3+} doping due to concentration quenching. For a better understanding of decay kinetics, the time-resolved emission spectrum (TRES) is shown in Fig. 4(c). The sharp-line emission (^2E) can be seen for longer delay times (~3 ms); however, the broadband emission ($^4T_2$) vanished at shorter delay times. Hence, the best fit of decay curves into the bi-exponential model and microsecond decay time suggested strong spin–orbit coupling (SOC) between $^4T_2$ and ^2E excited states of Cr^{3+} ions.[50]

2.4 Temperature-dependent PL studies

To evaluate thermal stability of the Cr^{3+}-doped YAGG phosphor, the temperature-dependent PL properties were investigated in detail. Fig. 5(a) displays the temperature-dependent PL emission spectra of the YAGG:0.04Cr^{3+} phosphor. The PL intensity of $^2E \rightarrow {}^4A_2$ (R-line) and phonon bands decreased gradually at elevated temperature; however, the PL emission band became broader at higher temperatures due to enhanced emission from the $^4T_2$ level (Fig. 5(b)). The total integral intensity ($^2E + {}^4T_2 \rightarrow {}^4A_2$) remains almost constant at elevated temperatures and nearly zero-thermal quenching was observed in the temperature range of 298 to 433 K (see Fig. 5(c) and (d)). The YAGG:0.04Cr^{3+} phosphor exhibits excellent thermal stability and maintained 105% of the initial emission intensity at 150 °C. The peak intensities at 690 ($^2E \rightarrow {}^4A_2$) and 750 nm (dominant $^4T_2 \rightarrow {}^4A_2$) as a function of temperature are shown in Fig. 5(e). The sharp-line emission intensity from the ^2E state decreased significantly (~67% at 423 K), while the intensity at 750 nm increased to 113% at 423 K. Hence, the increased broadband emission originating from $^4T_2 \rightarrow {}^4A_2$ compensates for the thermal quenching of PL intensity. Consequently, FWHM of the emission band increased significantly with increase in temperature (Fig. 5(f)).

We evaluated the activation energy for thermal quenching of the $^2E \rightarrow {}^4A_2$ emission band using the Arrhenius equation:[51]

$$I_T = I_0/(1 + A\exp(-\Delta E/kT)) \quad (5)$$

where I_0 and I_T are the integrated emission intensities at the initial (T_0) and given temperatures (T), respectively, ΔE denotes the activation energy for thermal quenching, k is the Boltzmann constant, and A is a constant. The E_a values were calculated by linear fit of experimental data in the $\ln[(I_0/I_T) - 1]$ *versus* $1/kT$ plot shown in Fig. 6(a). Two sections were observed with distinct ΔE values (0.38 eV and 0.166 eV) on different temperature scales. This revealed the prevalence of different thermal processes in different temperature ranges. At lower temperature, the energy barrier for thermal quenching is higher. However, with increase in temperature, a considerable lowering of the activation energy was noticed.

The configurational coordinate diagram of Cr^{3+} can be referred to get a better understanding of the thermal quenching behavior (Fig. 6(b)). The sharp line emission from the ^2E state is shown by $^2E \rightarrow {}^4A_2$ transition (process 1). In general, the thermal quenching mechanism of broadband emission originating from $^4T_2 \rightarrow {}^4A_2$ transition (process 2) is due to increased

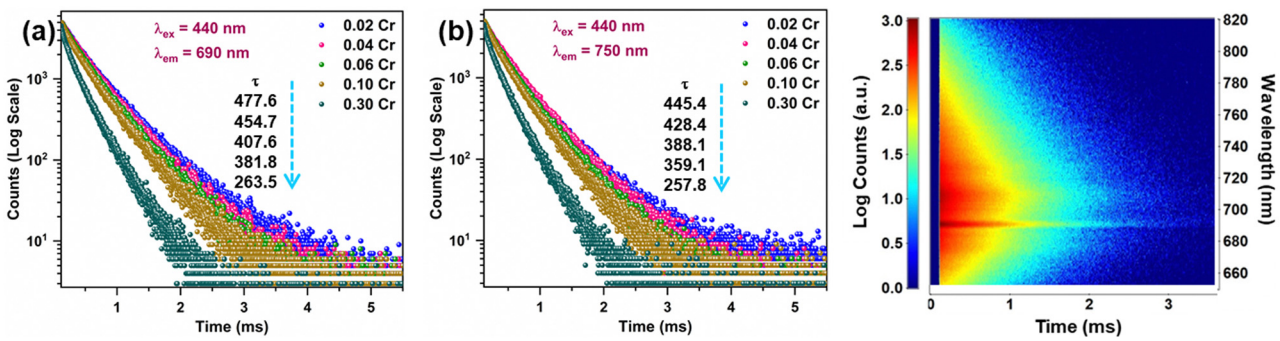

Fig. 4 Decay curves of YAGG:xCr^{3+} (x = 0.02–0.30 mol) phosphors monitored at (a) 690 nm and (b) 750 nm, upon 440 nm excitation, and (c) TRES spectra of the YAGG:0.04Cr sample under 440 nm excitation.

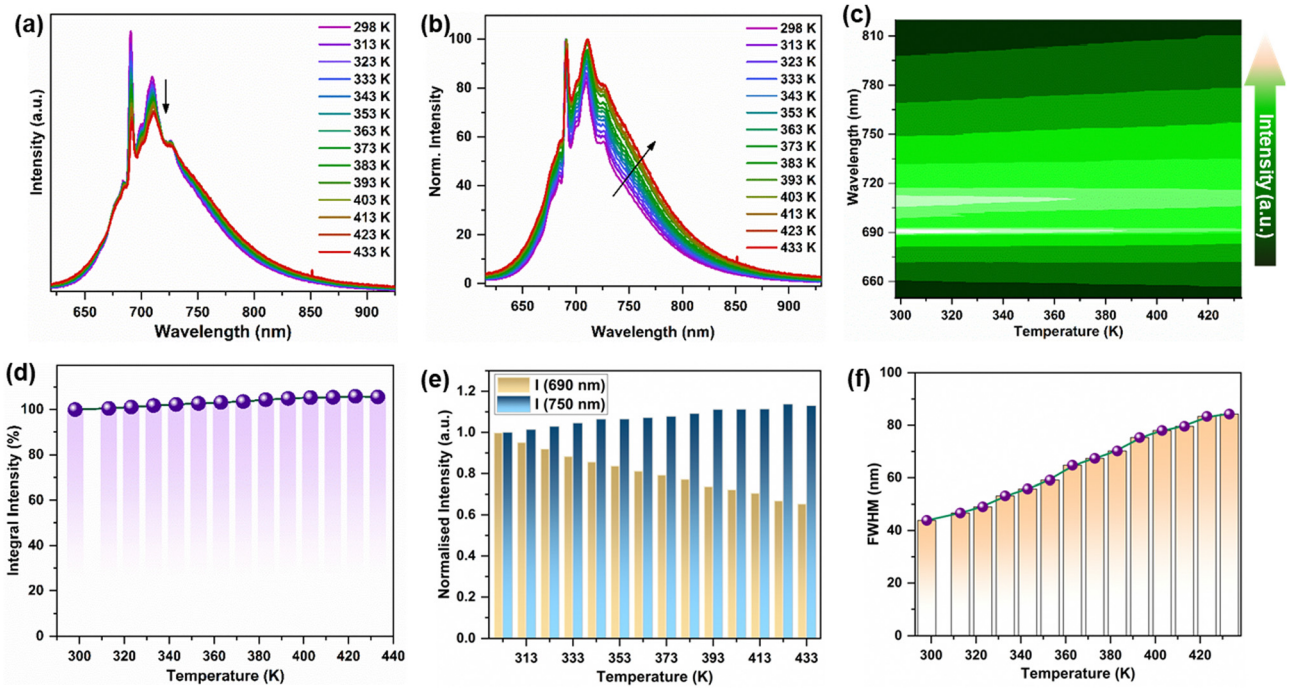

Fig. 5 (a) Temperature-dependent PL emission spectra of YAGG:0.04Cr^{3+} in the range of 298 to 433 K. (b) Normalised PL emission variation with temperature. (c) Contour plot of PL emission spectra at different temperatures. (d) Integral intensity at different temperatures. (e) Peak intensity for ^2E (690 nm) and $^4T_2$ (750 nm) as a function of temperature. (f) FWHM as a function of temperature.

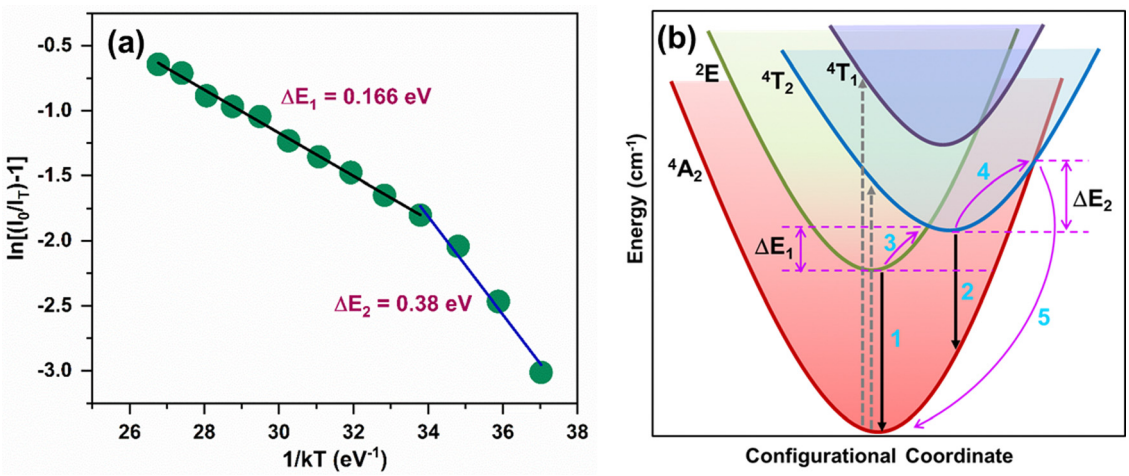

Fig. 6 (a) $\ln[(I_0/I_T) - 1]$ *versus* 1/kT plot. (b) Configuration coordinate diagram of the thermal quenching mechanism of the Cr^{3+}-doped YAGG matrix.

non-radiative loss at elevated temperatures. The electrons in the $^4T_2$ level may cross the intersection point of $^4T_2$ (excited state) and $^4A_2$ (ground state) with the energy barrier (ΔE_2) at higher temperatures. Consequently, the electron returns to $^4A_2$ states by nonradiative transitions that result in decreased intensity of $^4T_2 \rightarrow {}^4A_2$ emission (process 5).

Here, the thermal quenching mechanism of the sharp-line emission from the ^2E state (690 nm) is distinct from $^4T_2$, which can be observed by intensity changes at 750 nm. The different thermal quenching behaviour of the ^2E state from the $^4T_2$ state can be explained by the intersection between ^2E and ^4T states with lower activation energy due to intermediate crystal field strength. The thermal depopulation of the $^4T_2$ state is realized through a cross-over process from the $^4T_2$ to the $^4A_2$ state (process 4).[52] At high temperatures, the electrons can easily reach the intersection point of the ^2E and $^4T_2$ excited levels from the ^2E state in the case of intermediate crystal field strength, and this process (process 3) has an energy barrier denoted as ΔE_1 (where $\Delta E_1 < \Delta E_2$ for the intermediate crystal field). Following this, the electron can undergo radiative transition or non-radiative transition from $^4T_2$ excited levels to the ground state. Because of the thermal population of $^4T_2$ from the

^2E state, the broad $^4T_2 \rightarrow {}^4A_2$ emission can be enhanced at elevated temperatures. The above results can be further supported by the temperature-dependent lifetime study of $^4T_2 \rightarrow {}^4A_2$ and $^2E \rightarrow {}^4A_2$ transitions discussed in Section 2.6. The decrease of $^2E \rightarrow {}^4A_2$ lifetimes explains the abnormal anti-thermal quenching process of the broadband $^4T_2 \rightarrow {}^4A_2$ emission observed in this work. The weakening of the sharp-line emission (^2E) and the strengthened broad $^4T_2 \rightarrow {}^4A_2$ emission (Fig. 5(a) and (b)) revealed that thermal population of electrons in $^4T_2$ from the ^2E state may compensate for the non-radiative loss at higher temperatures. However, the enhanced $^4T_2 \rightarrow {}^4A_2$ broadband emission cannot be explained solely by thermal population. Therefore, the role of defects has been investigated thoroughly in the next section.

2.5 Role of defects in thermal stability and NIR PersL: experimental and theoretical investigation

We employed the PALS technique to understand the nature and density of defects in Cr^{3+}-doped YAGG phosphors. The fitting of positron annihilation lifetime spectra yielded three lifetimes in all the cases as shown in the typical fitting in Fig. S10a (ESI†). The longest lifetime was $\sim$1.5 ns and with an intensity of $<$0.5% but the inclusion of this component was necessary for best fit with χ^2 close to 1. This component is due to positronium formation on the surface of the powder particles and is well known and hence it is not discussed further. The other two positron lifetimes denoted as τ_1 and τ_2 in the increasing order of their magnitudes and the fractional intensity (I_1) corresponding to τ_1 ($I_2 \sim 100 - I_1$) are shown in Fig. S10b and c (ESI†). The intensity weighted average of the two positron lifetimes (τ_1) is also shown in Fig. S10b (ESI†). The first positron lifetime is from the delocalised bulk with some contribution from shallow positron traps like oxygen vacancies, while the second positron lifetime is from defects and surface annihilation of positrons. The first positron lifetime in undoped YAG is about 180 ps and is in good agreement with reported positron lifetimes of YAG based samples.[53,54] With increase in Cr^{3+} doping, the first positron lifetime reduced and reached minima at about 5% doping and it increased for the 15% doped sample. The second positron lifetimes are more than 400 ps for the undoped sample and reduced with Cr^{3+} doping, suggesting that the pre-existing large vacancy clusters near the surface of the particles anneal out in favour of isolated vacancies. The average positron lifetime decreased with increase in Cr^{3+} doping up to 5% doping and later increased. The intensity of positrons annihilating from delocalised states (I_1) showed minima at about 2% doping and showed drastic reduction in the 15% doped sample. The results obtained upon comparison with theoretically calculated positron lifetimes for various combinations of possible vacancies[55,56] suggest the formation of Al/Ga vacancies or aluminium/gallium vacancies associated with oxygen vacancies at higher concentration of Cr^{3+} doping.

For DFT calculations, we have considered cubic crystal structure with the space group $Ia\bar{3}d$ (space group number: 230) for $Y_3Al_2Ga_3O_{12}$ (Fig. 1(b)), where Ga^{3+}, Al^{3+} and Y^{3+} ions occupy the tetrahedral, octahedral and dodecahedral sites, respectively. The calculated lattice parameter is found to be 12.30 Å, which is close to the previously calculated and experimental values.[57–59] The calculated band gap is found to be 6.96 eV, which is in excellent agreement with the experimental value of 7.01 eV.[60] The density of states (DOS) plot for $Y_3Al_2Ga_3O_{12}$ in the absence of any defect is shown in Fig. 7(a). The valence band minimum (VBM) is mainly contributed by O (p) states with minor contribution from Y (p, d) and Ga (s, p, d). The bottom of the conduction band (CB) is mainly composed of Y (d) with minor Y (p), Ga (s, p), and O (p) states. The calculated defect formation energies of the defect containing $Y_3Al_2Ga_3O_{12}$ are provided in Table S4 (ESI†). It can be observed that formation of single vacancy follows the order, $V_O < V_{Ga} < V_{Al} < V_Y$. We have also considered vacancy clusters, containing cation–anion and cation–cation vacancies. The formation energy follows the order: $(V_{Ga}, V_O) < (V_{Al}, V_O) < (V_Y, V_O) < (V_{Ga}, V_{Al})$. Now, we proceed to discuss the influence of different types of defects on the electronic structure of $Y_3Al_2Ga_3O_{12}$. The DOS plots of $Y_3Al_2Ga_3O_{12}$ in the presence of different types of defects are shown in Fig. 7(b)–(f) and Fig. S11, S12 (ESI†). Fig. S13 (ESI†) shows the summary of the electronic structure description of all the defect containing systems. It can be seen from the DOS plots that the discrete impurity states in the forbidden region appear in the presence of all the vacancy defects, resulting in the formation of intermediate defect states between the valence band (VB) and CB.

Based on the above DFT and PALS results, we can conclude that the presence of oxygen vacancies (V_O) and oxygen vacancy–cation vacancy clusters in the YAGG matrix assisted in achieving excellent PL thermal stability. The DFT calculations suggested feasibility of V_O, V_{Ga}–V_O and V_{Al}–V_O cluster defect formation due to lowest defect formation energies. This is in good correlation with PALS lifetime results, which indicated the formation of cluster defects along with V_O formation due to high temperature sintering.

The Phonopy package[61] has been used for processing the data from VASP calculations to calculate the phonon spectra. Fig. S14 (ESI†) shows the phonon dispersion plot of $Y_3Al_2Ga_3O_{12}$. It can be observed that there exists no significant imaginary mode, indicating the dynamic stability of $Y_3Al_2Ga_3O_{12}$. This is expected since the garnet materials have been studied experimentally and reported to have high structural rigidity and thermal stability.[1]

To further characterize the trap depths and distribution, the TL studies were performed for the YAGG:0.04Cr^{3+} phosphor and the TL glow curve after charging with blue light (440 nm) for 100 s is displayed in Fig. 8(a). In the TL spectrum, the YAGG:0.04Cr^{3+} phosphor exhibited a broad TL band, which indicated a continuous distribution of traps in the range of 320 to 500 K. The deconvolution of the broad TL band provided three Gaussian peaks at 358, 394, and 458 K, respectively. The trap depth (E) can be evaluated using the following equation:

$$E = T_m/500 \quad (6)$$

where T_m represents the peak temperature (in K). The calculated trap depth values of the YAGG:0.04Cr^{3+} phosphor are 0.72, 0.82, and 0.91 eV. The three trap depths revealed the presence

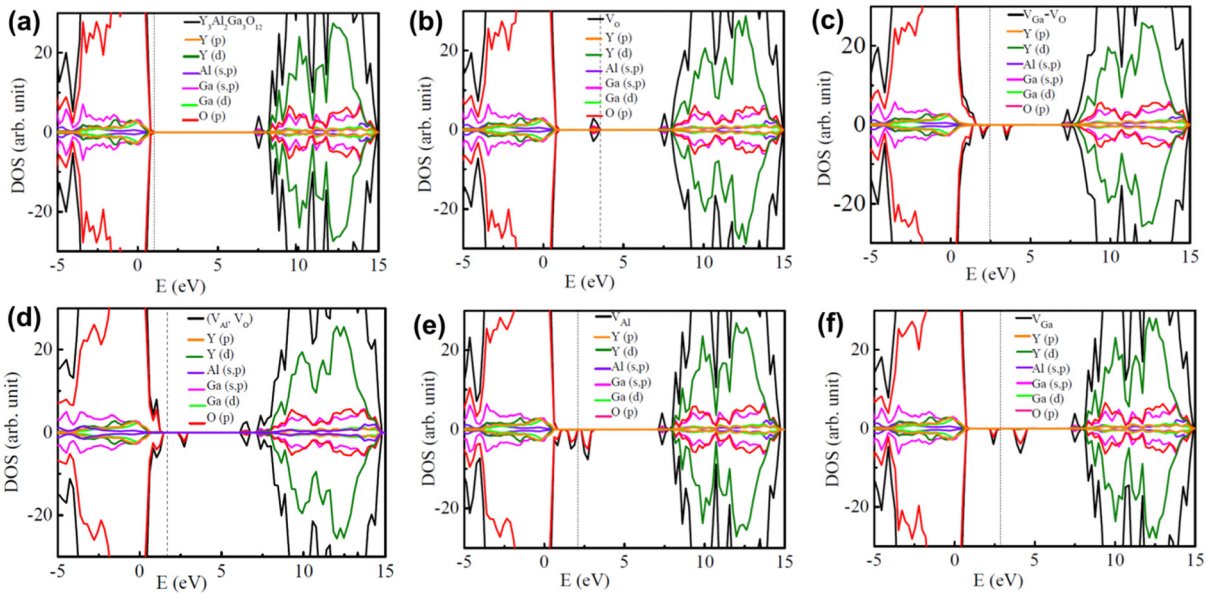

Fig. 7 (a) DOS of $Y_3Al_2Ga_3O_{12}$ and DOS of $Y_3Al_2Ga_3O_{12}$ in the presence of (b) one neutral oxygen vacancy, (c) neutral gallium and oxygen vacancies, (d) neutral aluminium and oxygen vacancies, (e) one neutral aluminium vacancy, and (f) one neutral gallium vacancy. The vertical dashed line indicates the Fermi level.

of both shallow and deep trap levels, which are located in between the valence band (VB) and conduction band (CB) of the YAGG:0.04Cr^{3+} phosphor. To verify the presence of V_O, the XPS study of the YAGG:0.04Cr^{3+} sample was carried out and the survey scan confirmed the presence of Y, Al, Ga, Cr and O elements (Fig. S15, ESI†). The XPS spectrum of O 1s is illustrated in Fig. 8(b). The Gaussian deconvolution of O 1s resulted in two peaks at ~530.2 and ~531.8 eV, which correspond to lattice oxygen of the sample and oxygen vacancies, respectively.[6,15]

The PersL decay curve was acquired after charging the YAGG:0.04Cr^{3+} phosphor with a 254 nm UV lamp for 2 min (Fig. 8(c)). The long PersL decay was observed and afterglow intensity was much higher than background even after 1 hour of decay, demonstrating the potential of YAGG:Cr^{3+} phosphors as efficient PersL materials.

Compiling the above results, possible mechanisms for defect induced thermal stability and PersL are proposed and illustrated in the schematic diagrams in Fig. 9(a) and (b), respectively. Fig. 9(c) and (d) demonstrate the schematic representation of V_O and (V_O–$V_{Al/Ga}$) cluster defects in the YAGG matrix, respectively. In summary, the thermal activation of NIR emission involving defect states can be divided into six parts based on earlier reports.[15,60] Firstly, the electrons of Cr^{3+} ions are excited to the $^4T_1$ (^4F) state by blue light excitation (440 nm) from the ground state, $^4A_2$ (process 1). It is noteworthy that electrons will not be reaching the CB upon blue light excitation, and thus, shallow traps will not be occupied during low energy excitation. Then, the electrons can relax back to lower energy excited states, $^4T_2$ (^4F) and ^2E by non-radiative pathways (process 2). This can be followed by processes 3 and 4, resulting in sharp-line and broadband NIR emission upon radiative transitions to the ground state. However, some of the electrons in excited states ($^4T_2$ (^4F) and ^2E) can be captured by deep traps such as V_O and cluster defects *via* tunnelling processes, as shown in process 5. The electrons cannot escape these deep

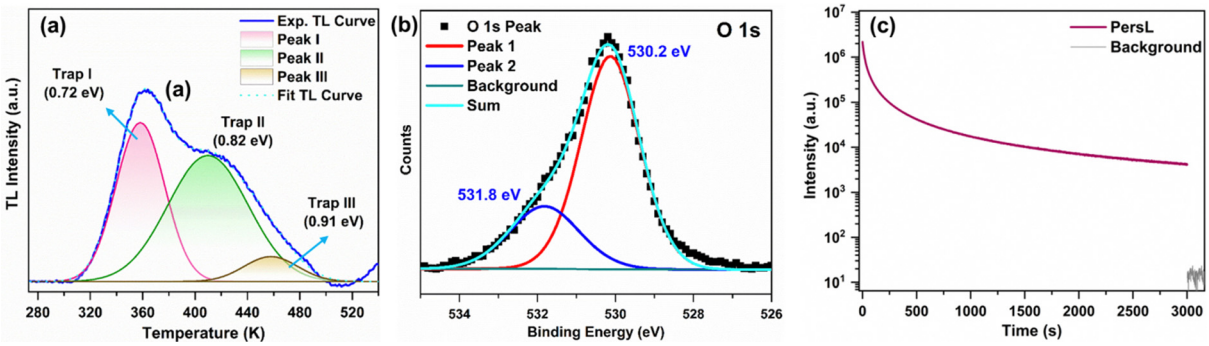

Fig. 8 (a) TL spectrum of the YAGG:0.04Cr^{3+} phosphor at room temperature upon charging with 440 nm light for 100 s, (b) O 1s XPS spectra of the YAGG:0.04Cr^{3+} phosphor, and (c) PersL decay curve under UV lamp (254 nm) charging for 2 min.

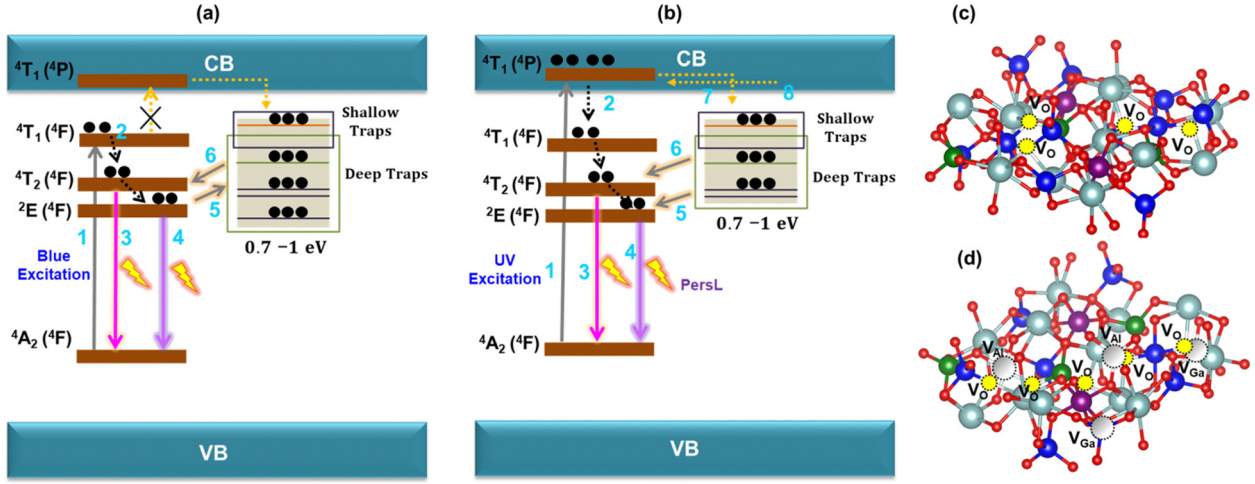

Fig. 9 Schematic representation of the mechanism of (a) defect induced thermal stability and (b) PersL. (c) and (d) Schematic representation of V_O and (V_O–$V_{Al/Ga}$) cluster defects in the YAGG matrix, respectively.

traps ($E > 0.8$ eV) at room temperature; however, thermal stimulation will provide activation energy required for detrapping of electrons from deep traps to Cr^{3+} excited energy levels (process 6). Thereafter, final transition to the ground state will result in enhanced emission intensities at higher temperatures.

Furthermore, using UV excitation to obtain PersL (Fig. 9(b)) will populate $^4T_1$ states and filling of traps through the conduction band is feasible (process 7). With time, the detrapping processes (process 8) and tunnelling of electrons (process 6) from deep traps will result in PersL of Cr^{3+} for a longer time.

Here, we could achieve thermally robust luminescence of Cr^{3+} ions and explain the role of structural rigidity and defects in the YAGG matrix. The quantum efficiency of the YAGG:Cr^{3+} matrix is quite high, ~76%. In order to balance the both, optimization of defect concentration is crucial for achieving high quantum efficiency and maintaining the loss of luminescence at elevated temperatures (not more than 3–4%). Defect engineering will be performed in the future to investigate the effect of defect density on the PLQY and achieve higher quantum yield for the thermally robust YAGG:Cr phosphor reported in this work.

2.6 Low temperature-dependent PL study and EXAFS investigation

The investigation of photophysical properties of Cr^{3+} ions at low temperatures can provide useful insights into the different radiative and non-radiative processes and temperature-dependent population of excited states ($^4T_2/^2E$). In order to explore the luminescence properties of Cr^{3+} at cryogenic temperatures, we recorded low temperature dependent PL emission spectra of the YAGG:0.04Cr^{3+} sample in the range of 80 to 300 K as shown in Fig. 10(a). The emission intensities as a function of temperature could be visualised in Fig. 10(b). The normalised PL emission spectrum at 80 and 300 K revealed considerable broadening of the emission band with diminished ^2E emission at room temperature (Fig. 10(c)). In this work, the Dq/B value of 2.37 falls into the regime of the intermediate crystal field, where $^4T_2$ and ^2E excited states lie within the reach of the intersection point between the $^4T_2/^2E$ excited states, with a very small ΔE_1 (Fig. 6(b)). The emergence of dominant sharp emission (^2E) at low temperature is in agreement with the thermal population of $^4T_2$ excited states from ^2E at elevated temperatures. Therefore, strong $^2E \rightarrow {}^4A_2$ emission is observed at low temperature and the broadband $^4T_2 \rightarrow {}^4A_2$ emission is attainable at higher temperatures. The normalised intensity PL emission spectra revealed similar increment in the FWHM of the emission band as observed at high temperatures (Fig. 10(d)). No prominent peak shifts were observed for the R-line and phonon bands. Fig. 10(e) depicts the variation in total integrated and peak intensities with temperature. The overall integrated intensity does not vary much with increase in temperature; however, the intensity of phonon sidebands decreased with temperature. The emission loss is compensated by increase in the broadband $^4T_2 \rightarrow {}^4A_2$ emission. The same can be supported by the decreased lifetime of the ^2E excited state at elevated temperatures. The decay curves under 440 nm excitation and monitoring 690 nm emission as a function of temperature are shown in Fig. 10(f). Decay curves monitored at 710 and 725 nm are presented in Fig. S16 (ESI†) and lifetime values are tabulated in Table S5 (ESI†), where a similar decrease in the lifetimes was observed.

To probe the local structure changes in the octahedral coordination of Cr^{3+} ions, low-temperature dependent EXAFS studies were carried out at the Ga K-edge as Cr^{3+} ions substitute Ga/Al octahedral sites. The temperature-dependent EXAFS measurements were conducted using a closed-cycle He cryostat, spanning a range from 16 to 300 K at the Ga K-edge of the YAGG:0.04Cr^{3+} sample in the transmission mode. Fig. 11(a) presents the XANES spectra from these temperature-dependent measurements, revealing a consistent oxidation state across the temperature spectrum. However, notable alterations are evident in the Fourier-transform EXAFS spectra, as depicted in Fig. 11(b). Specifically, the second and third coordination peaks (observed at 2.9 and 3.3 Å, respectively) exhibit an

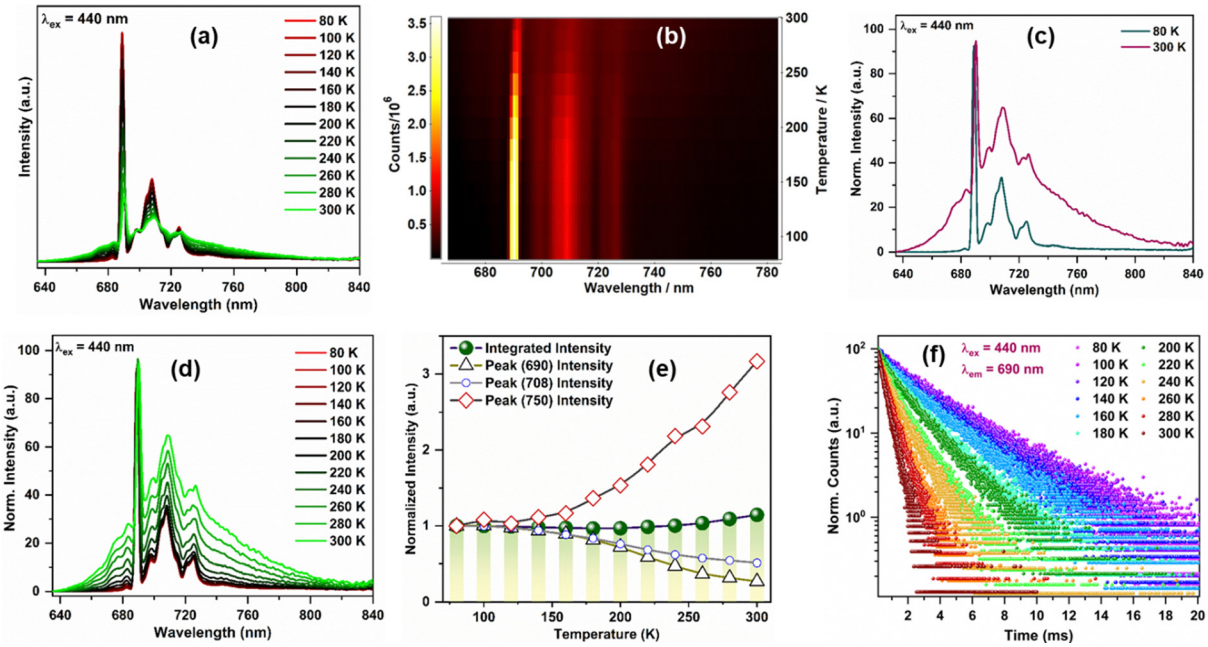

Fig. 10 (a) Low temperature-dependent PL emission spectra of YAGG:0.04Cr^{3+} in the range of 80 to 300 K. (b) Contour plot of PL emission spectra as a function of temperature. (c) Normalised PL emission at 80 and 300 K. (d) Normalised PL emission spectra at different temperatures. (e) Integral intensity at different temperatures and peak intensities at 690, 708, and 750 nm as a function of temperature. (f) Luminescence decay profiles in the temperature range of 80 to 300 K monitored at 690 nm under 440 nm excitation.

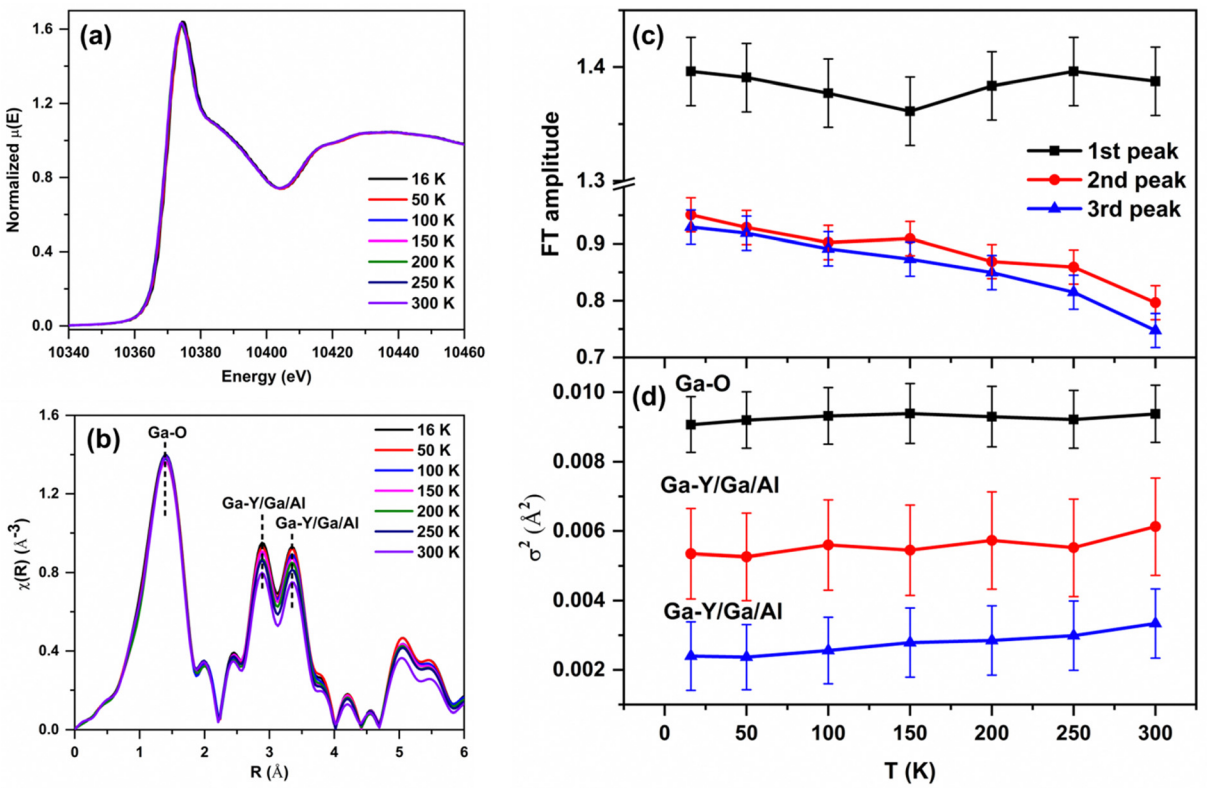

Fig. 11 (a) Temperature-dependent XANES spectra at the Ga K-edge. (b) Fourier transform EXAFS fittings of undoped and Cr^{3+} doped YAGG at the Ga K-edge for temperature-dependent measurements. (c) Variation of peak amplitude of three coordination peaks. (d) Variation of Debye–Waller factors of the corresponding coordination peaks with temperature.

augmentation in peak amplitude with decreasing temperature. This temperature-dependent variation appears to be a conventional thermal effect, devoid of any anomalous behavior across the temperature range.

An intriguing observation emerges regarding the nearly constant amplitude of the first coordination peak throughout the temperature range. This phenomenon could be attributed to the minimal vibrational activity induced by temperature changes in the octahedral coordination of Ga sites (GaO_6), particularly in proximity to neighboring atoms. The observed differences could be attributed to varying coupling levels. The robust coupling interaction between gallium (Ga) and oxygen (O) atoms may render the Ga–O coordination less susceptible to external influences. Conversely, the coordination with other atoms is characterized by greater distances from the Ga atoms, resulting in weaker coupling interactions. Consequently, the next-nearest–neighbor coordination and third-nearest–neighbor coordination are more prone to temperature-induced alterations due to their comparatively smaller coupling interactions. Fig. 11(c) illustrates the amplitude of all three peaks, corresponding to Ga–O and Ga–Y/Al/Ga coordinations, displaying a characteristic temperature-dependent pattern. Furthermore, the Debye–Waller factors obtained from the EXAFS fitting are shown in Fig. 11(d). Despite the presence of sizable error bars, a systematic trend is discernible with respect to temperature, indicative of underlying structural variations similar to the correlated Debye model.

The above results revealed rigidity of GaO_6 octahedral sites as the bond lengths remained intact without significant increase in the disorder values. This suggested that the substitution of rigid Al/GaO_6 sites by Cr^{3+} ions will result in less structural distortion as a function of temperature and thus assist in attaining the abnormal thermal quenching of NIR luminescence.

2.7 Applications

2.7.1 NIR LED fabrication. The NIR pc-LED device based on YAGG:0.04Cr^{3+} was fabricated using the 420 nm blue LED chip with the YAGG:0.04Cr phosphor. Fig. 12(a) shows the electroluminescence (EL) spectra of the YAGG:0.04Cr^{3+} phosphor and the images of a 420 nm LED and NIR pc-LED device emission (without/with a blue filter) in the inset. In order to demonstrate the potential of our device for night vision applications, the imaging performance was evaluated by capturing the photos of BARC logo and flowers in daylight (left panel) and under NIR pc-LED light (right panel) with a camera (Fig. 12(b)).

The power-dependent EL spectra of the fabricated NIR pc-LED are shown in Fig. 12(c) and (d). The EL emission intensity increased when the power is increased from 600 mW to 1200 mW (Fig. 12(e)). The slope of 1 obtained for logarithmic plot of intensity *versus* power revealed linear relation of EL intensity with power. Hence, the NIR pc-LED fabricated in this work displays superior optoelectronic properties, which can be utilized for night vision and other potential applications.

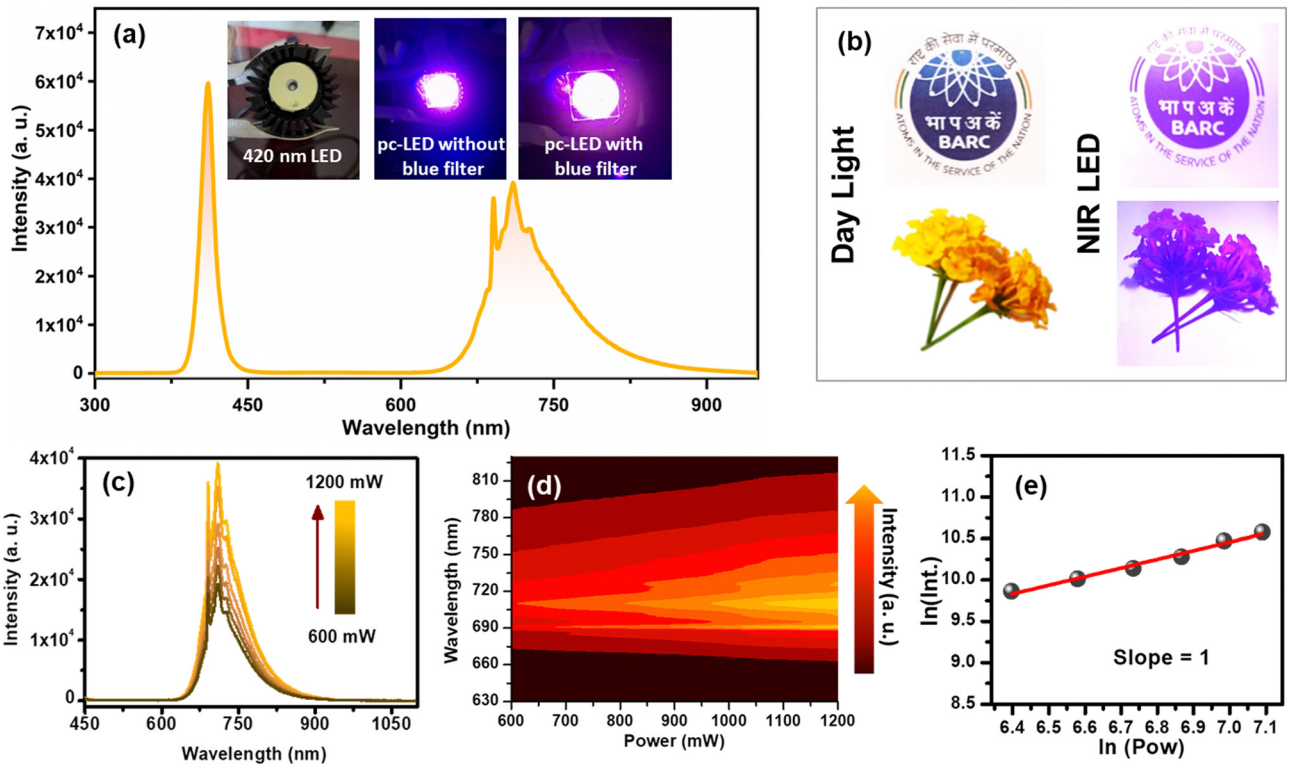

Fig. 12 (a) Electroluminescence (EL) spectra of the YAGG:0.04Cr^{3+} phosphor and the images of a 420 nm LED and NIR pc-LED device emission (without/with a blue filter), (b) photos of objects under daylight (left panel) and NIR light captured by a camera (right panel). (c) Power-dependent EL spectra of the fabricated YAGG:0.04Cr^{3+} NIR pc-LED. (d) Contour maps for intensity as a function of power. (e) Logarithmic plots of *I versus P*.

2.7.2 Thin film for NIR persistent luminescence. Thin film of YAGG:0.04Cr^{3+} phosphor/PMMA was fabricated and uniform dispersion of the material in PMMA was confirmed by elemental mapping (Fig. S17, ESI†). Fig. 13(a) shows the PL emission spectra of the thin film upon 440 nm blue light excitation. The inset displays the emission image of the thin film, and photographs of the thin film kept upon letters to show transparency of the fabricated thin film. The thin film fabrication imparted moisture stability to YAGG:0.04Cr^{3+} phosphor emission that was recorded after keeping the film in water for a day (Fig. S18, ESI†). Benefitting from large trap distribution observed in the TL spectrum, we investigated the persistent (PersL) luminescence of the thin film of the YAGG:0.04Cr^{3+} phosphor upon charging by X-rays for 1 minute. Fig. 13(b) presents the persistent luminescence decay curve of the YAGG:0.04Cr^{3+} phosphor and a NIR PersL for 2.5 hours was attained in this work. The NIR PersL can be utilized for night vision and imaging applications.

3. Experimental section

3.1 Synthesis

A series of YAGG:$x$$Cr^{3+}$ (x = 0.02, 0.04, 0.06, 0.10 and 0.30 mol) phosphors were synthesized by a high-temperature two step solid-state method. The raw materials, Y_2O_3 (99.99%), Al_2O_3 (AR), Ga_2O_3 (AR), and Cr_2O_3 (AR), were weighed in stoichiometric amounts and mixed homogeneously by grinding for 20 min using an agate mortar and pestle. Then, the fine mixture was calcined at 1200 °C for 15 h in a tubular furnace in air. Then, the powder was annealed at 1400 °C for 15 h in air after intermittent grinding for 15 min. After cooling, all the samples were ground well into fine powder for further measurements.

3.2 Fabrication of thin film

1.5 g of poly(methyl methacrylate) (PMMA) polymer (average M.W. ~15 000) was dissolved in toluene solution. Then, the YAGG:0.04Cr^{3+} powder was dispersed in solution and kept stirring overnight. The thin films were fabricated on a glass substrate by a drop casting method and left to dry at room temperature.

The characterization techniques, EXAFS experimental details, and computational details are provided in Sections S1, S2 and S3 in the ESI.†

4. Conclusions

In this work, we synthesized an efficient $Y_3Al_2Ga_3O_{12}$:Cr^{3+} NIR garnet phosphor, which exhibits broadband emission covering a range of 630–950 nm. The $Y_3Al_2Ga_3O_{12}$:Cr^{3+} phosphor displays thermally stable broadband NIR emission and at 150 °C, it maintains 105% of the intensity at room temperature. This material possesses a high internal quantum efficiency of 76%. EXAFS studies confirmed the octahedral coordination of Cr^{3+} ions and no significant changes were observed in bond lengths at higher Cr^{3+} content. EPR studies correlated well with EXAFS and an intense signal at $g \sim 3.75$ confirmed isolated Cr^{3+} ions in octahedral sites. Temperature dependent studies probed the structural changes of GaO_6 sites with temperature and revealed rigid octahedral sites. Furthermore, TL studies revealed large trap formation with a wide range of trap depths (~0.7 to 1 eV). The formation of oxygen vacancies (V_O) and cluster defects ($V_{Al/Ga}$–V_O) was affirmed by XPS and PALS studies, which facilitated the observed long PersL with UV charging (254 nm). DFT calculations revealed the lower formation energies of V_O and V_O–$V_{Ga/Al}$ cluster defects. The mechanism of defect activated thermal stability and PersL was established based on the experimental and theoretical calculations. Finally, an NIR pc-LED was fabricated, which displays efficient electroluminescence and can be utilized for potential applications in imaging and night vision. The thin film was fabricated using the YAGG:Cr^{3+} phosphor, which showed long PersL under X-ray charging.

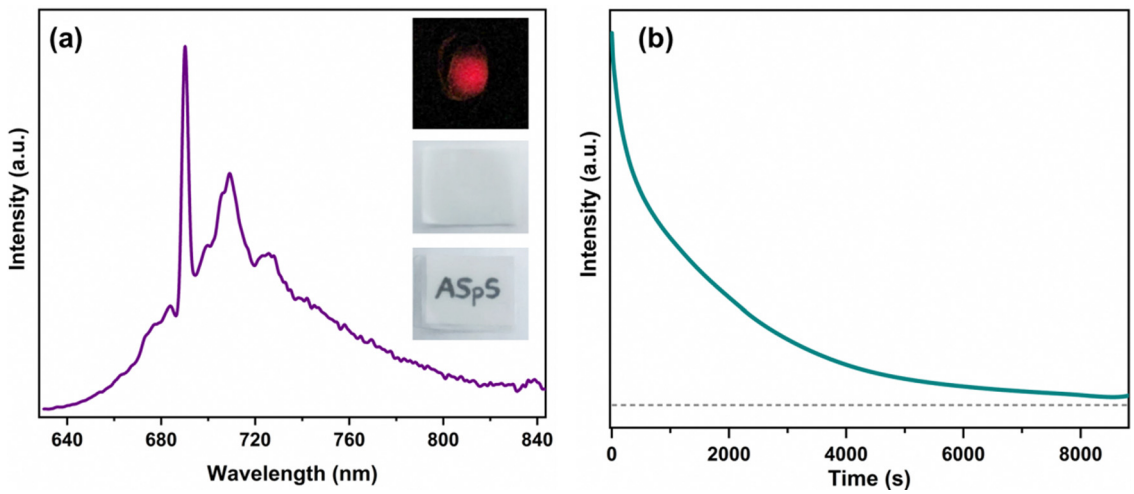

Fig. 13 (a) PL emission spectra of YAGG:0.04Cr^{3+}/PMMA film with the emission image and film photographs in the inset. (b) PersL decay curve of YAGG:0.04Cr^{3+} thin film under X-ray charging for 1 minute.

Conflicts of interest

There are no conflicts to declare.

Acknowledgements

A. Balhara and Santosh K. Gupta would like to thank Dr Biplab Ghosh, RRCAT for allotment of the EXAFS beamline and Dr Deepak Tyagi, BARC for help with XPS measurements. We would also like to acknowledge Dr Mohit Tyagi, BARC, for performing X-ray PersL measurements, Dr Manoj Kumar Gupta, AMPRI, for SEM analysis, and Dr Praveen Kumar, IACS, Kolkata for help with TEM measurements. This research is funded by Goverment of India through Department of Atomic Energy.

References

1 P. Dang, Y. Wei, D. Liu, G. Li and J. Lin, Recent advances in chromium-doped near-infrared luminescent materials: fundamentals, optimization strategies, and applications, *Adv. Opt. Mater.*, 2023, **11**(3), 2201739.

2 V. Rajendran, W.-T. Huang, K.-C. Chen, H. Chang and R.-S. Liu, Energy-saving chromium-activated garnet-structured phosphor-converted near-infrared light-emitting diodes, *J. Mater. Chem. C*, 2022, **10**(39), 14367–14378.

3 L. Zhang, D. Wang, Z. Hao, X. Zhang, G. H. Pan, H. Wu and J. Zhang, Cr^{3+}-doped broadband NIR garnet phosphor with enhanced luminescence and its application in NIR spectroscopy, *Adv. Opt. Mater.*, 2019, **7**(12), 1900185.

4 H. Jiang, L. Chen, X. Wu, Z. Luo, R. Li, Y. Liu, Z. Liu, P. Sun, W. You and J. Jiang, Spectral Regulation and Efficiency Optimization in Cr^{3+}-Doped Gadolinium Aluminum Gallium Garnet Near-Infrared Ceramic Phosphors *via* Crystal-Field Engineering, *Adv. Mater. Technol.*, 2022, **7**(12), 2200519.

5 X. Zou, X. Wang, H. Zhang, Y. Kang, X. Yang, X. Zhang, M. S. Molokeev and B. Lei, A highly efficient and suitable spectral profile Cr^{3+}-doped garnet near-infrared emitting phosphor for regulating photomorphogenesis of plants, *Chem. Eng. J.*, 2022, **428**, 132003.

6 T. Yang, H. Jiang, O. Hai, Y. Dong, S. Liu and S. Gao, Effect of Oxygen Vacancies on the Persistent Luminescence of $Y_3Al_2Ga_3O_{12}$:Ce^{3+},Yb^{3+} Phosphors, *Inorg. Chem.*, 2021, **60**(23), 17797–17809.

7 G. Liu and Z. Xia, Modulation of Thermally Stable Photoluminescence in Cr^{3+}-Based Near-Infrared Phosphors, *J. Phys. Chem. Lett.*, 2022, **13**(22), 5001–5008.

8 M.-H. Chan, W.-T. Huang, K.-C. Chen, T.-Y. Su, Y.-C. Chan, M. Hsiao and R.-S. Liu, The optical research progress of nanophosphors composed of transition elements in the fourth period of near-infrared windows I and II for deep-tissue theranostics, *Nanoscale*, 2022, **14**(19), 7123–7136.

9 H. Xiao, J. Zhang, L. Zhang, H. Wu, H. Wu, G. Pan, F. Liu and J. Zhang, Cr^{3+} activated garnet phosphor with efficient blue to far-red conversion for pc-LED, *Adv. Opt. Mater.*, 2021, **9**(20), 2101134.

10 D. Huang, S. Liang, D. Chen, J. Hu, K. Xu and H. Zhu, An efficient garnet-structured $Na_3Al_2Li_3F1_2$:Cr^{3+} phosphor with excellent photoluminescence thermal stability for near-infrared LEDs, *Chem. Eng. J.*, 2021, **426**, 131332.

11 H. Lin, G. Bai, T. Yu, M. K. Tsang, Q. Zhang and J. Hao, Site occupancy and near-infrared luminescence in $Ca_3Ga_2Ge_3O_{12}$:Cr^{3+} persistent phosphor, *Adv. Opt. Mater.*, 2017, **5**(18), 1700227.

12 Y. Zou, C. Hu, S. Lv, Y. Shao, B. Teng, F. You, H. Xu and D. Zhong, Realization of Broadband Near-Infrared Emission with High Thermal Stability in $YGa_3(BO_3)_4$:Cr^{3+} Borate Phosphor, *Inorg. Chem.*, 2023, **62**(48), 19507–19515.

13 J. Wang, Z. Lyu, G. Peng, D. Sun, S. Shen, Z. Lu, L. Wang, H. Zhao, S. Wei and H. You, Cr^{3+}-Doped NIR Phosphor with Well-Defined Stokes/Anti-Stokes Phonon Sidebands for a Ratiometric Thermometer and Thermally Stable NIR LEDs, *Chem. Mater.*, 2023, **35**(10), 3968–3975.

14 D. Chen, Z. Wan, Y. Zhou, X. Zhou, Y. Yu, J. Zhong, M. Ding and Z. Ji, Dual-Phase Glass Ceramic: Structure, Dual-Modal Luminescence, and Temperature Sensing Behaviors, *ACS Appl. Mater. Interfaces*, 2015, **7**(34), 19484–19493.

15 S. Ding, P. Feng, J. Cao, X. Ma and Y. Wang, Multiple coordination of chromium ion luminescence: a strategy for designing ultra-broadband NIR long persistent luminescent materials, *ACS Appl. Mater. Interfaces*, 2022, **14**(39), 44622–44631.

16 L. Yao, Q. Shao, M. Shi, T. Shang, Y. Dong, C. Liang, J. He and J. Jiang, Efficient ultra-broadband Ga_4GeO_8:Cr^{3+} phosphors with tunable peak wavelengths from 835 to 980 nm for NIR pc-LED application, *Adv. Opt. Mater.*, 2022, **10**(4), 2102229.

17 Q. Zhang, X. Wei, J. Zhou, B. Milićević, L. Lin, J. Huo, J. Li, H. Ni and Z. Xia, Thermal stability improvement of Cr^{3+}-activated broadband near-infrared phosphors *via* state population optimization, *Adv. Opt. Mater.*, 2023, **11**(14), 2300310.

18 F. Xiao, C. Xie, S. Xie, R. Yi, H. Yuan and H. Zhou, Multi-site Cr^{3+} occupation-related broadband NIR luminescence in Cr^{3+}-doped $Li_3Mg_2NbO_6$, *CrystEngComm*, 2021, **23**(33), 5585–5594.

19 K. Sudarshan, A. Balhara, M. S. Kambli, R. T. Parayil, S. M. Patil and S. K. Gupta, Multiple local site Cr^{3+} emission leading to broadband NIR light in novel $SrGa_2O_4$ phosphors, *Mater. Res. Bull.*, 2024, **169**, 112537.

20 F. Zhao, Z. Song and Q. Liu, Advances in chromium-activated phosphors for near-infrared light sources, *Laser Photonics Rev.*, 2022, **16**(11), 2200380.

21 L. Huang, L. Lin, W. Xie, Z. Qiu, H. Ni, H. Liang, Q. Tang, L. Cao, J.-X. Meng and F. Li, Near-infrared persistent luminescence in a Cr^{3+}-doped perovskite for low-irradiance imaging, *Chem. Mater.*, 2020, **32**(13), 5579–5588.

22 O. Taktak, H. Souissi and S. Kammoun, Optical properties of the phosphors Zn_2SnO_4:Cr^{3+} with near-infrared long-persistence phosphorescence for bio-imaging applications, *J. Lumin.*, 2020, **228**, 117563.

23 L. Jiang, X. Jiang, C. Wang, P. Liu, Y. Zhang, G. Lv, T. Lookman and Y. Su, Rapid discovery of efficient long-

wavelength emission garnet: Cr NIR phosphors *via* multi-objective optimization, *ACS Appl. Mater. Interfaces*, 2022, **14**(46), 52124–52133.

24 Y. Wang, Z. Wang, G. Wei, Y. Yang, S. He, J. Li, Y. Shi, R. Li, J. Zhang and P. Li, Ultra-Broadband and high efficiency Near-Infrared $Gd_3Zn_xGa_{5-2x}Ge_xO_{12}:Cr^{3+}$ (x = 0–2.0) garnet phosphors *via* crystal field engineering, *Chem. Eng. J.*, 2022, **437**, 135346.

25 C. Cai, S. Liu, F. Zhao, H. Cai, Z. Song and Q. Liu, Inducing octahedral distortion to enhance NIR emission in Cr-doped garnet $Ca_3(Al,Sc)_2Ge_3O_{12}$, *J. Mater. Chem. C*, 2023, **11**(25), 8462–8469.

26 Z. Jia, C. Yuan, Y. Liu, X.-J. Wang, P. Sun, L. Wang, H. Jiang and J. Jiang, Strategies to approach high performance in Cr^{3+}-doped phosphors for high-power NIR-LED light sources, *Light: Sci. Appl.*, 2020, **9**(1), 86.

27 Q. Zhang, G. Li, P. Dang, D. Liu, D. Huang, H. Lian and J. Lin, Enhancing and tuning broadband near-infrared (NIR) photoluminescence properties in Cr^{3+}-doped $Ca_2YHf_2Al_3O_{12}$ garnet phosphors *via* Ce^{3+}/Yb^{3+}-codoping for LED applications, *J. Mater. Chem. C*, 2021, **9**(14), 4815–4824.

28 Y. Wang, M. Shang, Y. Sun, M. Deng, X. Xing, P. Dang and J. Lin, Highly efficient and thermally stable broadband near-infrared emitting garnet $Ca_3Sc_2Ge_3O_{12}:Cr^{3+}$,Ce3+ phosphors for multiple pc-LED applications, *J. Mater. Chem. C*, 2023, **11**(27), 9291–9299.

29 H. Li, J. Jiao, X. Xiang, J. Wu, W. Hu, J. Xie, S. Huang, H. Zhang and J. Zhu, Directly Identifying Multiple Cr^{3+} Emitting Centers for Broad Near-Infrared Emission in an Efficient and Near-Zero Thermal Quenching Garnet-Type Phosphor, *Adv. Opt. Mater.*, 2024, 2302391.

30 C. Li and J. Zhong, Highly efficient broadband near-infrared luminescence with zero-thermal-quenching in garnet $Y_3In_2Ga_3O_{12}:Cr^{3+}$ phosphors, *Chem. Mater.*, 2022, **34**(18), 8418–8426.

31 V. Boiko, Z. Dai, M. Markowska, C. Leonelli, C. Mortalò, F. Armetta, F. Ursi, G. Nasillo, M. L. Saladino and D. Hreniak, Particle size-related limitations of persistent phosphors based on the doped $Y_3Al_2Ga_3O_{12}$ system, *Sci. Rep.*, 2021, **11**(1), 141.

32 Q. Du, J. Ueda and S. Tanabe, Toward color variation of long persistent luminescence in Pr^{3+}-doped garnet transparent ceramic phosphors, *J. Mater. Chem. C*, 2023, **11**(46), 16225–16233.

33 M. Qiang, Y. Tang, S. Ye, W. Lou, J. Chao, H. Lin and D. Zhang, Novel YAGG:Cr garnet phosphor ceramic with broadband near infrared (NIR) emission and luminescence thermal stability for plant growth, *Ceram. Int.*, 2024, **50**(3), 4823–4830.

34 J. Ueda, S. Miyano and S. Tanabe, Formation of deep electron traps by Yb^{3+} codoping leads to super-long persistent luminescence in Ce^{3+}-doped yttrium aluminum gallium garnet phosphors, *ACS Appl. Mater. Interfaces*, 2018, **10**(24), 20652–20660.

35 J. Xu, J. Ueda, Y. Zhuang, B. Viana and S. Tanabe, $Y_3Al_{5-x}Ga_xO_{12}:Cr^{3+}$: A novel red persistent phosphor with high brightness, *Appl. Phys. Express*, 2015, **8**(4), 042602.

36 V. Laguta, Y. Zorenko, V. Gorbenko, A. Iskaliyeva, Y. Zagorodniy, O. Sidletskiy, P. Bilski, A. Twardak and M. Nikl, Aluminum and Gallium Substitution in Yttrium and Lutetium Aluminum–Gallium Garnets: Investigation by Single-Crystal NMR and TSL Methods, *J. Phys. Chem. C*, 2016, **120**(42), 24400–24408.

37 V. Boiko, M. L. Saladino, F. Armetta, F. Ursi, M. Markowska, K. Grzeszkiewicz, C. Mortalò, C. Leonelli and D. Hreniak, Urea Glass Route as a Way to Optimize YAGG:Ce^{3+},Cr^{3+},Pr^{3+} Nanocrystals for Persistent Luminescence Applications, *Langmuir*, 2022, **38**(38), 11539–11549.

38 E. Arroyo, B. T. Herrero, J. M. de la Fuente, M. Ocaña and A. I. Becerro, Highly uniform $Y_3Al_2Ga_3O_{12}$-based nanophosphors for persistent luminescence bioimaging in the visible and NIR regions, *Inorg. Chem. Front.*, 2022, **9**(11), 2454–2461.

39 Z. Dai, V. Boiko, K. Grzeszkiewicz, M. Markowska, F. Ursi, J. Hölsä, M. L. Saladino and D. Hreniak, Effect of annealing temperature on persistent luminescence of $Y_3Al_2Ga_3O_{12}:Cr^{3+}$ co-doped with Ce^{3+} and Pr^{3+}, *Opt. Mater.*, 2021, **111**, 110522.

40 F. Farges, Chromium speciation in oxide-type compounds: application to minerals, gems, aqueous solutions and silicate glasses, *Phys. Chem. Miner.*, 2009, **36**, 463–481.

41 A. M. Beale, D. Grandjean, J. Kornatowski, P. Glatzel, F. M. de Groot and B. M. Weckhuysen, Unusual coordination behavior of Cr^{3+} in microporous aluminophosphates, *J. Phys. Chem. B*, 2006, **110**(2), 716–722.

42 A. Pantelouris, H. Modrow, M. Pantelouris, J. Hormes and D. Reinen, The influence of coordination geometry and valency on the K-edge absorption near edge spectra of selected chromium compounds, *Chem. Phys.*, 2004, **300**(1–3), 13–22.

43 M. L. Peterson, G. E. Brown Jr and G. A. Parks, Direct XAFS evidence for heterogeneous redox reaction at the aqueous chromium/magnetite interface, *Colloids Surf., A*, 1996, **107**, 77–88.

44 R. D. Shannon, Revised effective ionic radii and systematic studies of interatomic distances in halides and chalcogenides, *Acta Crystallogr., Sect. A: Cryst. Phys., Diffr., Theor. Gen. Crystallogr.*, 1976, **32**(5), 751–767.

45 B. B. Srivastava, S. K. Gupta and Y. Mao, Remarkable enhancement of photoluminescence and persistent luminescence of NIR emitting $ZnGa_2O_4:Cr^{3+}$ nanoparticles, *CrystEngComm*, 2020, **22**(14), 2491–2501.

46 B. B. Srivastava, S. K. Gupta, S. Mohan and Y. Mao, Molten-Salt-Assisted Annealing for Making Colloidal $ZnGa_2O_4$:Cr Nanocrystals with High Persistent Luminescence, *Chem. – Eur. J.*, 2021, **27**(44), 11398–11405.

47 Y. Zhang, S. Miao, Y. Liang, C. Liang, D. Chen, X. Shan, K. Sun and X.-J. Wang, Blue LED-pumped intense shortwave infrared luminescence based on Cr^{3+}–Yb^{3+}-*co*-doped phosphors, *Light: Sci. Appl.*, 2022, **11**(1), 136.

48 Y. Wang, Z. Wang, G. Wei, Y. Yang, S. He, J. Li, Y. Shi, R. Li, J. Zhang and P. Li, Highly efficient and stable near-infrared broadband garnet phosphor for multifunctional phosphor-

converted light-emitting diodes, *Adv. Opt. Mater.*, 2022, **10**(11), 2200415.

49 W. Nie, Y. Li, J. Zuo, Y. Kong, W. Zou, G. Chen, J. Peng, F. Du, L. Han and X. Ye, Cr^{3+}-activated $Na_3X_2Li_3F_{12}$ (X = Al, Ga, or In) garnet phosphors with broadband NIR emission and high luminescence efficiency for potential biomedical application, *J. Mater. Chem. C*, 2021, **9**(42), 15230–15241.

50 X. Dai, X. Zou, H. Zhang, W. Chen, C. Yang, M. S. Molokeev, Z. Xia, Y. Liu, X. Zhang and M. Zheng, Novel Cr^{3+}-Doped Garnet Phosphor with Broadband Efficient Far-Red Emission for Photochrome Matching Plant-Lighting, *Adv. Opt. Mater.*, 2023, 2302380.

51 A. Balhara, S. K. Gupta, M. Abraham, B. Modak, S. Das, C. Nayak, H. V. Annadata and M. Tyagi, Trap engineering through chemical doping for ultralong X-ray persistent luminescence and anti-thermal quenching in Zn_2GeO_4, *J. Mater. Chem. C*, 2024, **12**(5), 1728–1745.

52 K. Elzbieciak-Piecka and L. Marciniak, Optical heating and luminescence thermometry combined in a Cr^{3+}-doped $YAl_3(BO_3)_4$, *Sci. Rep.*, 2022, **12**(1), 16364.

53 P. Husband, I. Bartošová, V. Slugeň and F. Selim, In Positron annihilation in transparent ceramics, *J. Phys.: Conf. Ser.*, 2016, 012013, IOP Publishing.

54 F. Selim, C. Varney, M. Tarun, M. Rowe, G. Collins and M. McCluskey, Positron lifetime measurements of hydrogen passivation of cation vacancies in yttrium aluminum oxide garnets, *Phys. Rev. B: Condens. Matter Mater. Phys.*, 2013, **88**(17), 174102.

55 A. Marinopoulos, First-principles study of the formation energies and positron lifetimes of vacancies in the Yttrium-Aluminum Garnet $Y_3Al_5O_{12}$, *Eur. Phys. J. B*, 2019, **92**, 1–9.

56 F. Selim, D. Winarski, C. Varney, M. Tarun, J. Ji and M. McCluskey, Generation and characterization of point defects in $SrTiO_3$ and $Y_3Al_5O_{12}$, *Results Phys.*, 2015, **5**, 28–31.

57 Z. Li, B. Zhong, Y. Cao, S. Zhang, Y. Lv, Z. Mu, Z. Hu and Y. Hu, Energy transfer and tunable luminescence properties in $Y_3Al_2Ga_3O_{12}$:Tb^{3+},Eu^{3+} phosphors, *J. Alloys Compd.*, 2019, **787**, 672–682.

58 C. Linderälv, D. Åberg and P. Erhart, Luminescence quenching *via* deep defect states: A recombination pathway *via* oxygen vacancies in Ce-doped YAG, *Chem. Mater.*, 2020, **33**(1), 73–80.

59 J. H. Yoder and M. Keith, Complete substitution of aluminum for silicon: The system $3MnO\cdot Al_2O_3\cdot 3SiO_2$—$3Y_2O_3\cdot 5Al_2O_3$, *Am. Mineral.*, 1951, **36**(7–8), 519–533.

60 J. Xu, D. Murata, J. Ueda, B. Viana and S. Tanabe, Toward rechargeable persistent luminescence for the first and third biological windows *via* persistent energy transfer and electron trap redistribution, *Inorg. Chem.*, 2018, **57**(9), 5194–5203.

61 A. Togo and I. Tanaka, First principles phonon calculations in materials science, *Scr. Mater.*, 2015, **108**, 1–5.

